INFORMATION TO USERS

This manuscript has been reproduced from the microfilm master. UMI films the text directly from the original or copy submitted. Thus, some thesis and dissertation copies are in typewriter face, while others may be from any type of computer printer.

The quality of this reproduction is dependent upon the quality of the copy submitted. Broken or indistinct print, colored or poor quality illustrations and photographs, print bleedthrough, substandard margins, and improper alignment can adversely affect reproduction.

In the unlikely event that the author did not send UMI a complete manuscript and there are missing pages, these will be noted. Also, if unauthorized copyright material had to be removed, a note will indicate the deletion.

Oversize materials (e.g., maps, drawings, charts) are reproduced by sectioning the original, beginning at the upper left-hand corner and continuing from left to right in equal sections with small overlaps. Each original is also photographed in one exposure and is included in reduced form at the back of the book.

Photographs included in the original manuscript have been reproduced xerographically in this copy. Higher quality 6" x 9" black and white photographic prints are available for any photographs or illustrations appearing in this copy for an additional charge. Contact UMI directly to order.

UMI®

Bell & Howell Information and Learning
300 North Zeeb Road, Ann Arbor, MI 48106-1346 USA
800-521-0600

Université d'Ottawa · University of Ottawa

Study of Lanthanum-based Cathode Materials for Organic Light Emitting Devices

Timothy C. Gorjanc

January 19, 1999

Thesis

Submitted to the University of Ottawa

in partial fulfillment of the requirements for the degree of

Master's in Physics

Abstract

Since the dawn of the information age, the high technology industry has been driven to display more data and to create large area high-resolution displays. Display devices based on the cathode ray tube are often bulky and consume large amounts of power. More recently, liquid crystal display technology has dominated the display market. However, when compared to cathode ray tubes they are at a disadvantage due to their extremely high price and low viewing angle performance. Plasma-based displays have also entered the foray but have the disadvantage of extremely high price (several tens of thousands of dollars) and extremely high power consumption and heat emission.

Organic light emitting diodes, introduced in the late 1980s, are emerging as an attractive alternative to these other display technologies. These devices offer cheap materials, low operating voltages, high brightness and a wide viewing angle. The ability to spin coat molecular materials on large rigid or flexible substrates is unparalleled in existing technologies.

Several different device geometries are possible, ranging from the simple homostructure, where there is only one organic material present, to the complex microcavity, where dielectric stacks are used to selectively filter out specific wavelengths of light. No matter which geometry is chosen, all of these devices have several common features: a high work function anode (usually transparent) and a low work function cathode. Due to the low work function requirement of the cathode, we are limited to the very reactive metals in the periodic table. In this thesis cathodes based on pure lanthanum, lanthanum-silver bilayers, and lanthanum-yttrium alloys were investigated.

Heterostructure devices were chosen for this study due to the increased luminescence efficiency of the heterojunction over the homostructure.

Organic light emitting devices were fabricated using high vacuum sublimation. Four sets of devices were investigated; three based on an indium tin oxide (ITO) anode and one based on a palladium anode. The ITO devices had either lanthanum, lanthanum-yttrium alloy, or lanthanum-silver bilayer cathodes. The palladium device was based on a lanthanum cathode. The ITO on glass substrates were obtained from a commercial supplier, while the palladium on glass substrates were fabricated immediately prior to device deposition. Primary device characterization included current-luminance-voltage and electro-luminescence measurements. When possible, Auger electron spectroscopy, scanning electron microscopy, atomic force microscopy, and x-ray photoelectron spectroscopy were performed on the devices to examine the quality of the interfaces and composition of the devices. It was found that lanthanum cathodes gave the best luminance results (~1200 cd/m^2 at ~16 V), although devices based on lanthanum-yttrium alloys gave similar results. Lanthanum-silver bilayer cathodes yielded the poorest results with high current densities and inhomogeneous light emission. The palladium based devices had severe shorts and poor light emission, which was due to a discontinuous palladium film and degassing of hydrogen when the device was placed under bias.

List of Figures

List of Tables

List of Abbreviations

Alq_3	*8-hydroxyquinolate aluminum*
AFM	*Atomic Force Microscopy*
AES	*Auger Electron Spectroscopy*
EL	*Electroluminescence*
ETL	*Electron Transport Layer*
ETM	*Electron Transport Material*
FEM	*Field Emission Scanning Electron Microscopy*
HOMO	*Highest Occupied Molecular Orbital*
HTL	*Hole Transport Layer*
HTM	*Hole Transport Material*
ITO	*Indium Tin Oxide*
LUMO	*Lowest Unoccupied Molecular Orbital*
OLED	*Organic Light Emitting Device*
PL	*Photoluminescence*
SCL	*Space Charge Limited*
SEM	*Scanning Electron Microscopy*
TCL	*Trap Charge Limited*
T_g	*Glass Transition Temperature*
TPD	*Tri-Phenyl Diamine*
XPS	*X-ray Photoelectron Spectroscopy*

To my parents, Marjan and Maria,

whose support and generosity

made all of this possible

Statement of Originality

To the best of my knowledge, the work carried out at the Institute for Microstructural Sciences at the National Research Council of Canada under the supervision of Dr. Marie D'Iorio is unique. Literature searches have not revealed any publications reporting the use of lanthanum-based cathodes for use in organic light emitting devices.

The work that was done involved the design, growth, and characterization of these devices. Additionally, some work performed during the last year is not presented as part of this thesis. Deposition and characterization of novel small molecules and polymeric materials relating to other projects and ion beam sputtering of indium tin oxide thin films were performed. I have designed a computer controlled current-luminance-voltage characterization system, performed photoluminescence measurements on samples from our collaborators, helped in the installation of new laboratory equipment and general operation of the clean room.

Early results of this thesis were presented at the 43rd Annual Meeting of the SPIE in San Diego, California, in July 1998. The submitted manuscript has been accepted for publication in the conference proceedings.

Acknowledgements

This thesis is the result of 15 months of work. I am grateful and indebted to a number of people for their assistance, suggestions, and stimulating discussions.

I would like to thank the Epitaxy Group in the Institute for Microstructural Sciences at the National Research Council Canada for providing me a second home while performing research for this thesis and for financial support.

To Don Brown, whose great patience and superb handiwork were tested on several occasions by my ignorance and incompetence.

To Margaret Buchanan for giving me her blessing (and help) to work in her lab.

To Irwin Sproule and Simona Moisa for their patience and quick processing of samples and spending time analyzing the results. To Jeff Fraser for performing the SEM and FEM imaging and to John McCaffrey for performing the AFM measurements.

To Brian Williams for his use of elastic bands, paper clips, magnets and wood pencils in the lab and to his attitude towards physics. Good luck in your retirement, you will be missed.

To Renée Harling, for giving me moral support and putting up with me in the weeks prior to completing this work.

To Ye Tao for his expertise, many stimulating conversations and trying to locate the source of the mystery odours that invade our lab from time to time.

To Jennifer Lam, my officemate, for giving me company during those long experiments and sending me a steady supply of humour, Chinese candy, and coffee.

To Christophe Py for introducing me to clean room etiquette and for helpful discussions.

To Mr. MacGregor who first exposed me to physics and taught me that physics is about not only equations, but also visualizing and understanding.

To Dr. B. A. Logan, who made me realize my love and passion for physics and converted me from a confused first year Chemical Engineering student to a dedicated Physics student.

To Dr. A. K. S. Song and Dr. I. L'Heureux for exposing me to statistical mechanics and solid state physics and for being excellent and inspiring teachers.

To Dr. E. Fortin, Carla Miner and Iain Calder for exposing me to semiconductor physics and showing me that physicists can find employment in their field outside of academia.

Finally, to my supervisor and friend, Marie D'Iorio, who helped guide me to this end. For her supervision, academic, financial, and moral support, I am eternally grateful.

Table of Contents

1. Introduction

The first study of electroluminescence in an organic material was documented in 1963[1]. A faint glow from a thin film of anthracene shaved from a single bulk crystal was observed when a high voltage was applied. Organic materials were first considered for practical electroluminescent devices in the late 1960s by Dresber[2] but this was abandoned because of the high voltages required, low conductivity, and the great difficulty involved in growing large single crystals.

In 1987, Tang and Van Slyke[3] revitalized the field by developing an organic electroluminescent device based on 8-hydroxyquinolate aluminum which exhibited efficient production of green light. The field of organic electroluminescent devices has expanded exponentially in the following years offering cheap materials, large scale deposition, and bright electroluminescence coupled with a low turn-on voltage (>800 cd/m^2 @ 5.5V cw, ~ 4.5 Mcd/m^2 @ 10.5V pulsed[4]) over a wide spectral range. These devices are therefore an attractive alternative to current LCD, plasma and CRT displays. Molecular solids and polymers have also been used in the fabrication of transistors, laser diodes, and waveguides.

Understanding the underlying physics is critical in the design of a device that will have a low turn-on voltage as well as increased reliability and lifetime. One of these issues, which this work will focus on, is that of the cathode material and the cathode-organic interface. In previous work at the Institute for Microstructural Sciences[5], it was shown that lanthanum, despite its rapid oxidation, could be used as a cathode and that alloying with yttrium provided a stable cathode material. This thesis will expand on this work by examining these two material systems in detail as well as other lanthanum-metal

combinations. Injection mechanisms, contacts, and the formation of carbides and oxides at the cathode interfaces will also be discussed. The experimental work in this thesis involved the selection of the various cathode materials, etching of the substrate, growth, and, finally, characterization and analysis of the devices.

Chapter 2 will introduce organic light emitting devices in terms of structure, carrier transport, luminescence, and degradation processes. Details involving contact and surface effects at the metal-organic interfaces, as well as general material properties, will also be addressed. Chapter 3 will detail the experimental procedures. Chapter 4 will present results on the surface morphology of ITO and how it pertains to device performance. Electrical and optical properties of various devices will be analyzed and compared. Compositional analysis (AES and XPS) will be presented when possible along with scanning electron microscope images to give some qualitative results. Finally, we will summarize and give conclusions in Chapter 5.

2. Introduction to Organic Light Emitting Diodes

2.1 The Organic Heterostructure

In inorganic semiconductors, charge transport is band-like in nature and recombination of electrons and holes results in interband emission of light. Organic films, however, are amorphous and charge transport occurs via variable range hopping[6,7]. The carriers have polaron characteristics due to the softness of the lattice and recombination occurs in localized molecular excited states which results in excitonic emission[6,7]. These localized excited states are Frenkel excitons as opposed to extended state Wannier excitons.

A typical heterostucture device is shown in Figure 2.1. The organic materials can consist of long chain polymers, oligomers, or small molecules[3,8-10]. The molecular structure of the hole transport material (HTM) and the electron transport/emitting material (ETM) are shown in Figure 2.2. The anode is usually a high work function material that is transparent in the visible region. Usually, indium-tin-oxide (ITO)[3] is used, although other alternative materials such as palladium[5], nickel oxide, vanadium oxide, and iridium oxide[11] have been used. The high ionization potential of the organic material allows efficient charge injection from the ITO into the lowest unoccupied molecular orbital (LUMO) of the hole transport layer. The LUMO level is analogous to the valence band in semiconductors. This yields a higher hole mobility in the hole transport material thus allowing transport of holes injected from the anode to the hole/electron transport layer interface for recombination to occur. A triphenyl diamine derivative, TPD, is typically used as the hole transport material, although other materials such as NPB are possible[12]. The emitting layer, which also serves as the electron

transport layer, carries electrons from the cathode to the organic interface and mediates the recombination process. The low electron affinity of the electron transport layer (ETL) allows efficient electron injection from the low work function cathode into the ETL's highest occupied molecular orbital (HOMO) level. The HOMO level is analogous to the conduction band in semiconductors. Typical electron transport/emitting materials include Alq_3, Inq_3 and many others[3,13,14]. These HTL and ETL materials form a heterojunction, providing a barrier, to prevent the electrons/holes from traveling to the anode/cathode

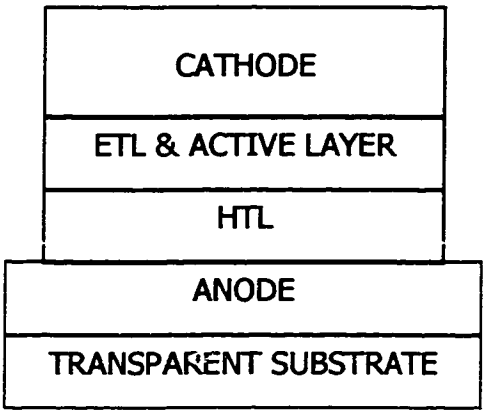

Figure 2.1: Schematic diagram of a typical organic heterostructure LED. The electron transport layer (ETL) is intrinsically n-type. The hole transport layer (HTL) is intrinsically p-type. The cathode is typically a low work function metal and the anode is a high work function, transparent metal.

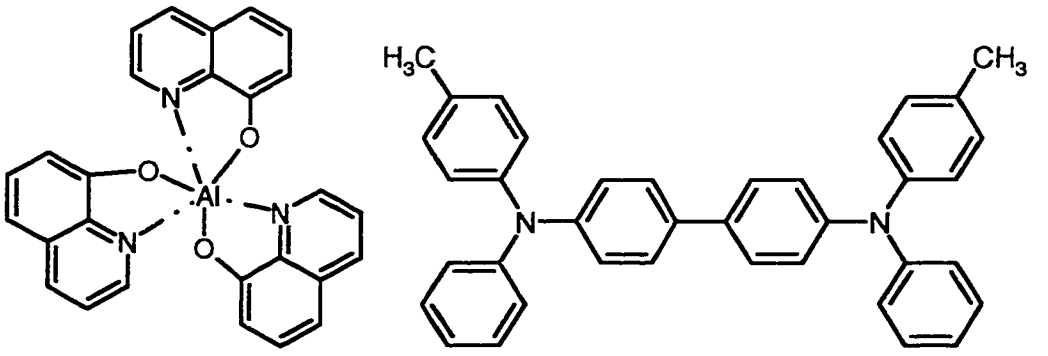

Alq_3 TPD

Figure 2.2: 8-hydroxyquinolate aluminum (Alq_3) emitter and ETL. N,N'-diphenyl-N,N'-(3-methylphenyl)-1,1'-biphenyl-4,4'diamine (TPD) HTL.

(see Figure 2.3). The first generation of devices used a Mg:Ag alloy (10:1)[13], Al or Ca[15] as cathodes; however these metals are either reactive (Mg, Ca) or have less than ideal work functions (Al, Ag), thus requiring high operating voltages and encapsulation techniques are required for acceptable device lifetimes.

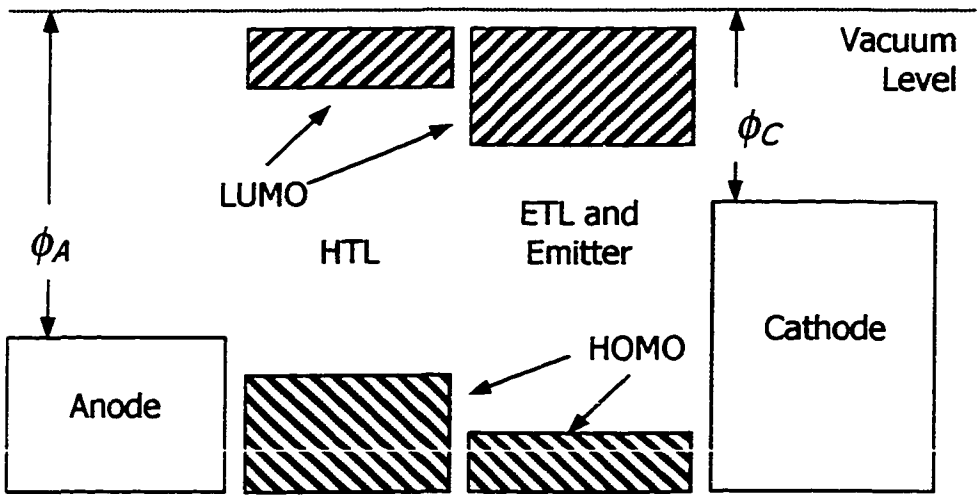

Figure 2.3: Detailed energy diagram of an organic heterostructure LED with no applied bias. The highest occupied molecular orbital (HOMO) and lowest unoccupied molecular orbital (LUMO) are analogous to the conduction and valence bands in inorganic semiconductors. ϕ_C is the cathode work function and ϕ_A is the anode work function. All energies are measured with respect to the vacuum level. The diagram is not drawn to scale.

2.2 Carrier Injection and Transport

2.2.1 Tunneling and Variable Range Hopping

Carrier can move between two molecules that are separated by a potential barrier in one of two ways: tunneling through or travelling over (via an activated state) the barrier. If the carrier travels over the barrier, the process is an activated process, such as variable range hopping. The variable range hopping model proposed by Mott[16] for non-crystalline semiconductors gives qualitative agreement with experimental results. It assumes that the Fermi energy lies within the localized state energy levels. The hopping distance has a $T^{-1/4}$ dependence and can be written as:

$$R^* = \left[\frac{2}{3}\pi\alpha N(E_F)kT\right]^{-1/4}, \tag{2.1}$$

where α is the carrier's wavefunction decay, $N(E_F)$ is the density of states at the Fermi energy, k is Boltzmann's constant and T is the temperature. The conductivity may then be written as[17]:

$$\sigma = \sigma_o T^{-1/2} \exp\left(-\frac{T_o}{T}\right)^{1/4}, \tag{2.2}$$

where $T_o \approx 7.64\alpha^3/kN(E_F)$ and $\sigma_o = A\nu_{ph}[N(E_F)/\alpha]^{1/2}$. A is a constant and ν_{ph} is the frequency of phonons involved in the hopping process.

2.2.2 Space Charge and Trapped Charge Limited Currents

The theory of space charge limited currents in insulating solids was first proposed by Rose[18] and extended by Lampert[19] to include trap effects which is referred to as trapped charge limited (TCL) current. Observation of the power law dependence of current on voltage was made by Smith and Rose[20]. At low operating voltages, carriers are captured in traps below the LUMO level (see Figure 2.4). As the bias is increased, more carriers are injected into the organic material and the traps are filled. The reduction of empty traps results in a rapid increase in the effective carrier mobility and therefore a rapid increase in the current. At extremely high injection levels, all of the traps become filled and the current then enters the SCL regime.

The theory of TCL conduction assumes, however, that energy bands exist in the material in question. This implies that the motion of carriers over many lattice sites can occur without interruption by deep trap levels. Most organic materials used for OLEDs have an extremely low density of thermally generated free charge carriers n_o (of the order

of 10^{10} cm^{-3}) along with low carrier mobility. As mentioned above, these are the conditions necessary for hopping transport.

At low voltages, we expect low-mobility ohmic conduction to dominate. This occurs via thermally generated free carriers. Here the current density is given by:

$$J_{\Omega} = q\mu_n n_o V/d\,, \tag{2.3}$$

where q is the electronic charge, μ_n is the electron mobility, n_o is the thermally generated background free charge density, V is the applied voltage, and d is the thickness of the ETL. If n_o is small compared to the injected charge density n_{inj} and the Fermi level lies below the trap energies, an SCL current is observed with a current density[21]

$$J_{SCL} = \frac{9}{8}\mu_n \varepsilon \frac{V^2}{d^3}, \tag{2.4}$$

where ε is the permittivity. This is known as Child's Law and is expected to dominate at low voltages and for thicker films.

At high injection currents, the current is governed by the density and energy distribution of the traps. Assuming an exponential trap distribution, the current density for electron injection in Alq_3 can be written as[21]:

$$J_{TCL} = N_{LUMO}\mu_n q^{(1-m)}\left(\frac{\varepsilon m}{N_t(m+1)}\right)^m \left(\frac{2m+1}{m+1}\right)^{(m+1)} \frac{V^{m+1}}{d^{2m+1}}, \tag{2.5}$$

where $m = T_t/T$, T_t is the trap temperature, T is the ambient temperature and N_{LUMO} is the density of states in the LUMO band.

Using equations 2.4 and 2.5, we may find the voltage at which we expect all of the traps to be filled and enter the SCL current regime and write it as:

$$V_{TCL-SCL} = \frac{n_o q d^2}{\varepsilon}\left(\frac{n_o}{N_{LUMO}}\right)\left(\frac{N_t}{n_o}\right)^m\left[\frac{9}{8}\left(\frac{m+1}{m}\right)^m\left(\frac{m+1}{2m+1}\right)^{m+1}\right]^{1/m-1}, \qquad (2.6)$$

In these types of devices, one can consider the existence of two different SCL regimes, one in the low- to mid-voltage regime and one in the high voltage regime. In the former, deep traps will collect injected electrons, creating a space charge region. As these traps are filled, the TCL regime is entered. Once all of the traps are filled, the second SCL regime is entered.

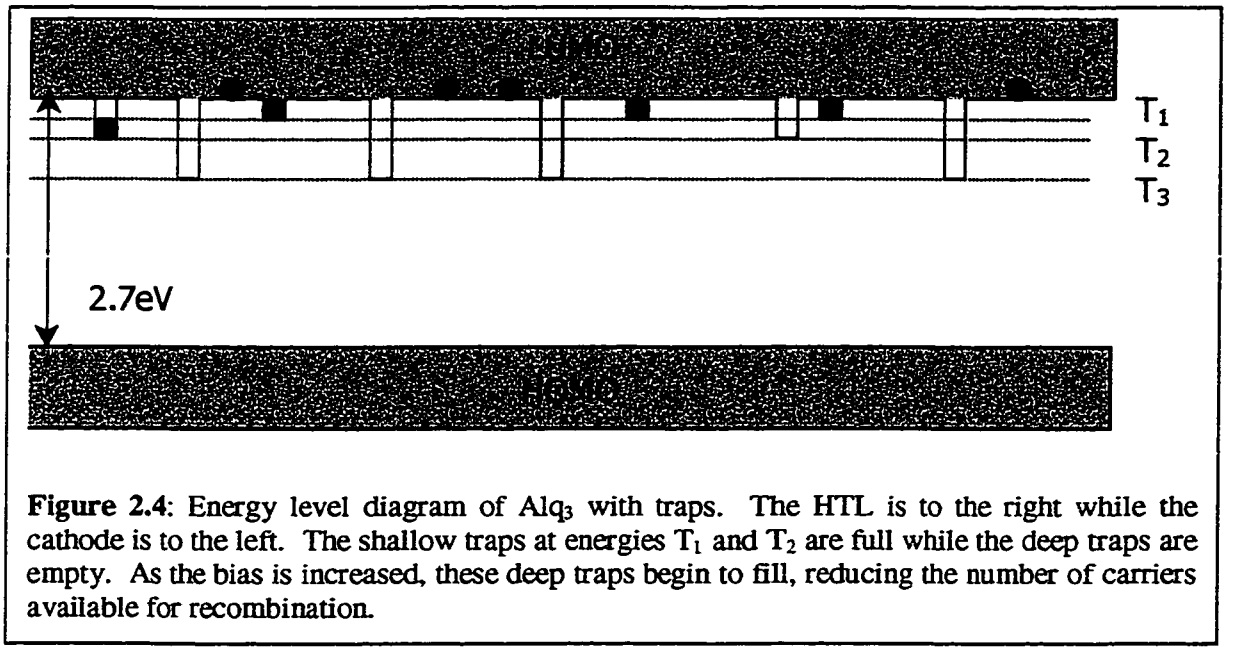

Figure 2.4: Energy level diagram of Alq_3 with traps. The HTL is to the right while the cathode is to the left. The shallow traps at energies T_1 and T_2 are full while the deep traps are empty. As the bias is increased, these deep traps begin to fill, reducing the number of carriers available for recombination.

2.2.3 Other Models

There have been other injection mechanisms proposed which give inconsistent results when compared to TCL injection. Some of the more common ones are[22]:

(a) Field assisted thermionic injection over the image force barrier[23]:

$$J \propto F^{3/4}\exp\left(aF^{1/2}\right), \quad with \quad a = (kT)^{-1}\left(e^3/4\pi\varepsilon_o\varepsilon\right)^{1/2}, \qquad (2.7)$$

(b) Tunneling through a triangular barrier (Fowler-Nordheim tunneling)[24,25]:

$$J \propto F^2 \exp(-b/F), \quad with \quad b = (2m^*)^{1/2}(8\pi/3he)\chi_b^{3/2}, \tag{2.8}$$

(c) Primary (hot) carrier penetration in the medium over the image force barrier[26,27]:

$$J \propto \exp\left(-c/F^{1/2}\right), \text{ with } c = (2\pi/h)(em^* \chi_c/2\pi\varepsilon_o\varepsilon)^{1/2} = l^{-1}(e/16\pi\varepsilon_o\varepsilon)^{1/2}, \tag{2.9}$$

Here, F denotes the electric field strength, m^* is the effective mass of the carriers within the barrier, χ_b and χ_c stand for the energy barriers for charge injection and l is the mean free path of the carriers. Kalinowski *et al.* have shown[22] that semi-log plots of J against $F^{1/2}$, F^{-1} and $F^{-1/2}$ yield straight lines within the suitable field ranges and the characteristic parameters a, b, and c can be extracted from the slope which, in turn, can give the barrier heights and the mean free path.

2.3 Luminescence

Recombination in the organic materials leads to the formation of excitons. Of these excitons, approximately 75% of them will be in the triplet state while the remainder will be in the singlet state. Triplet excitons are not desirable since they do not lead to optical radiation. Brown *et al.*[28] have determined that the theoretical maximum EL quantum yield is only 25% of the PL quantum yield.

In a singlet state there is no net electronic spin angular momentum whereas in a triplet state there is a net positive electron spin angular momentum and the molecule is paramagnetic. A triplet state lies at a lower energy than the corresponding excited singlet state. Optical transitions between triplet states and a singlet ground state are multiplicity forbidden and are therefore weak, while transitions between singlet states are usually strong. The decay of a triplet state occurs after a long time, with a half life of the order of 10's of milliseconds. This process is called phosphorescence. Fluorescence occurs when

an excited singlet state decays to the ground state where the half life is of the order of 10's of nanoseconds. Figure 2.5 gives a graphical depiction of the transitions and Figure 2.6 shows the PL spectra of the organic materials in powder form and the EL spectrum of a typical OLED device. It is evident that the light emitted from the OLED while under bias has the same spectral characteristics as the light emitted by Alq_3 in PL measurements.

In our analysis, we shall assume that the electroluminescence originates in the Alq_3 layer. The optical properties of low-mobility organic solids are dominated by Frenkel excitons. These excitons are formed by electrons that are localized around the traps and holes which are injected from the HTL. Radiative recombination then occurs

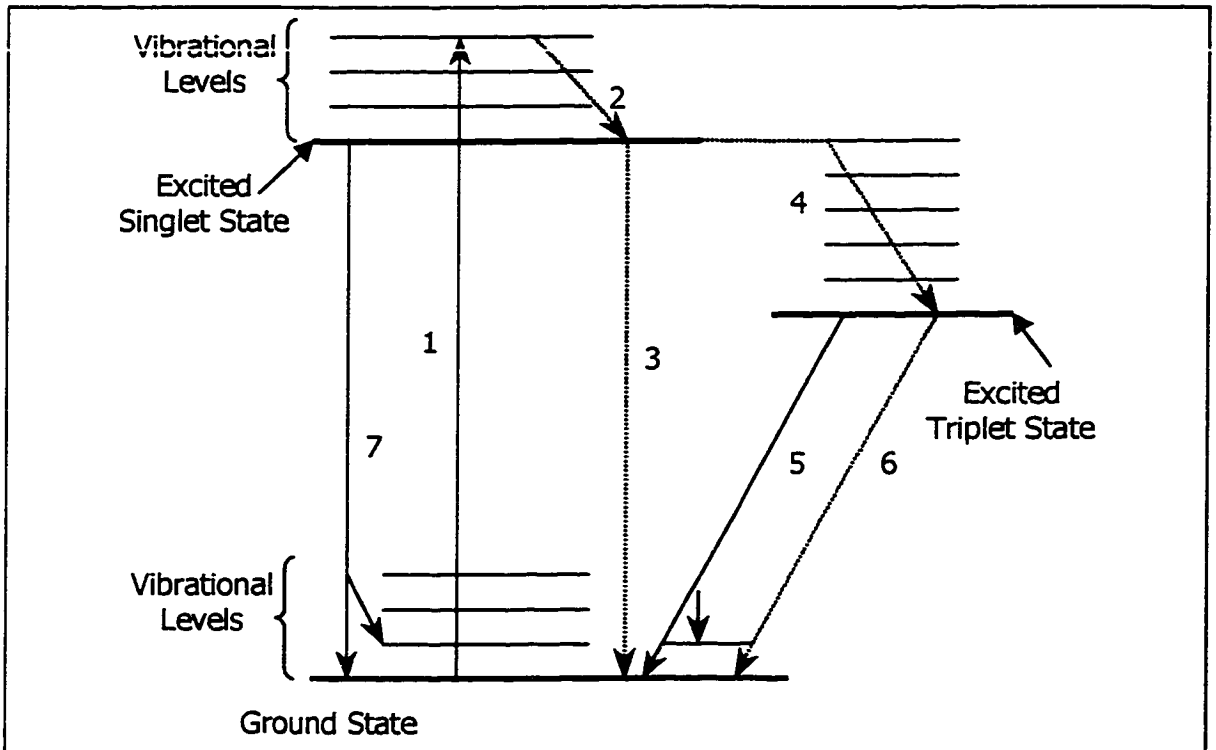

Figure 2.5: Radiative and non-radiative excitonic transitions in molecular solids. In our case, process 1 is achieved by the injection of electrons and holes and the formation of excitons in the Alq_3 layer. The vibrational levels are due to the vibrational modes of the molecules. Solid lines (5 and 7) indicate radiative transitions while dotted lines (2, 3, 4 and 6) indicate non-radiative transitions. From Guttmann and Lyons[7].

primarily in a region within a hole diffusion length (approximately 400Å) from the heterojunction in the Alq_3.

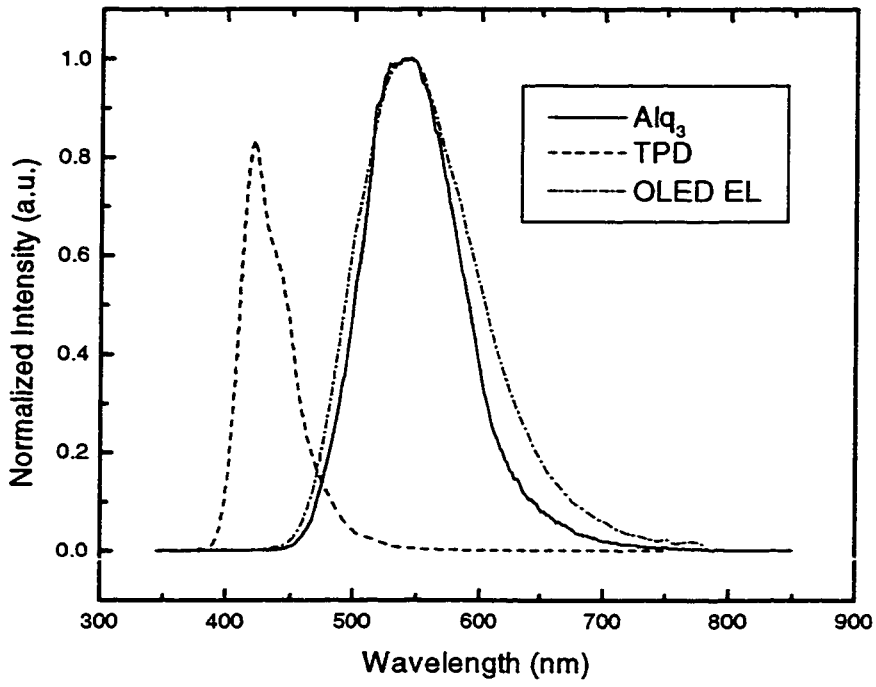

Figure 2.6: Room temperature PL of Alq_3 and TPD in powder form. The excitation source was a HeCd laser at 325nm. Also shown is the electroluminescence (EL) spectrum of a typical OLED used in this study. It is obvious that the emission from the OLED is originating in the Alq_3.

The electroluminescence flux, Φ_{EL}, is proportional to the rate of radiative recombination from these localized states, which in turn is proportional to the rate of recombination of minority carriers (holes) in the Alq_3 layer. It has been shown[14] that Φ_{EL} can be written as:

$$\Phi_{EL} = \alpha \eta_{PL}(T) p(d) \mu_p F(d), \tag{2.10}$$

where $F(d)$ is the electric field at the organic heterojunction, μ_p is the hole mobility, η_{PL} is the temperature dependent photoluminescence efficiency, and α is an efficiency factor including losses which do not exhibit significant temperature dependence. The hole density at the organic heterojunction is denoted as $p(d)$ and can be written as:

$$p(d) = N_{HOMO} \exp\left[\left(E_{HOMO} - E_p\right)/kT\right], \tag{2.11}$$

where E_p is the hole quasi-Fermi level and N_{HOMO} is the density of states in the HOMO level.

Kalinowski *et al.* have shown[22] that the EL intensity can be approximated fairly well with a power law of the form:

$$\Phi_{EL} \propto J^n, \tag{2.12}$$

with $n > 1$. It is based on the injection-controlled EL operation mode and requires that the recombination time be greater than the average transit time of the injected charge carriers.

The maximum theoretical external quantum efficiency of a device can be expressed as[29]:

$$\Phi_{EL} = \chi \Phi_F \eta_r \eta_e \leq \frac{1}{4} \times 1 \times 1 \times \frac{1}{2n^2}, \tag{2.13}$$

where χ is the fraction of recombinations that result in singlet excitons, Φ_F is the fraction of singlet excitons that emit, η_r is the fraction of electrons and holes that recombine in the emissive layer, and η_e is the fraction of emitted photons that escape from the device. As stated in section 2.3, it is thought that χ is about ¼ due to the relative spin degeneracy of singlet and triplet excitons. Φ_F and η_r can be as high as unity if conditions are favorable, while η_e is limited by internal reflection of photons emitted above the critical angle to

escape the substrate thus contributing to significant waveguide losses. Typical external quantum efficiencies are of the order of 2-4%.

Quenching of the emitted light due to high concentrations of organic materials is also a hindrance and must be considered during device design[30,31]. If the emission spectrum of the active material overlaps with the absorption spectrum of another material present within the device Förster energy transfer between molecules will occur[32]. Thermally activated exciton diffusion[33] also contribute to quenching the light output.

2.4 Degradation Processes

2.4.1 Introduction

There exist three major degradation modes in a double heterostructure OLED: the formation of black, non-emissive spots; abrupt ceasing of light emission associated with catastrophic failures due to electrical shorts; and long term wear-out associated with a decrease in quantum efficiency and luminance combined with an increase in voltage, while the device is under constant current. Since the recombination site is relatively far away from either electrode, Joule heating due to high electric fields and quenching of the emissive species by the electrodes has a trivial effect in the normal operating voltage regime. It has also been shown that the performance of laser diodes based on organic materials shows very little, if any, temperature dependence[34].

2.4.2 Dark Spot Formation

It is thought that dark spots originate as bright, high current areas in the device. When large area OLEDs are fabricated, there is a tendency for the formation of microscopic conduction pathways through the device resulting in shorts. These shorts are

typically burnt out when a high current (several tens of milliamps) is applied to the device. The presence of these shorts suggests that some type of non-planarity exists at either or both of the metal-organic interfaces. This may lead to non-uniform electric fields within the device and result in the formation of hot spots.

Burrows *et al.*[35] have thoroughly investigated the formation of dark spots in OLEDs and have suggested that these formations were a result of high current areas in the device. Once formed, dark spots increase in size leading to total device failure. Furthermore, these holes pass completely through the electrode. In the area surrounding these holes, it was noted that there was some delamination between the cathode and the Alq_3.

Antoniadis *et al.*[36] have also investigated the degradation mechanisms involved in OLEDs. They proposed that dark spots are pinholes in the cathode material in which water and oxygen can enter the device and affect the organic molecules. Particles and other imperfections existing on the ITO surface or introduced during device fabrication are prime candidates for pinhole formation. The growth rate of the pinholes was found to be dependent on relative humidity levels and devices with pinholes exhibit PL, suggesting that the organic materials below are chemically intact.

2.4.3 Catastrophic Failure

It is thought that devices undergo catastrophic failure due to reactions at the electrode-organic interfaces. When the device is exposed to an external bias for an extended period of time, blisters may form characteristic of local melting of the organic material. It has been suggested that a layer of 1000Å of polyanilene (PANI:CSA)[36] or a relatively thin layer of copper phthalocyanine (CuPc)[37] can be inserted between the ITO

and TPD layers to smooth the interface and promote continuous film formation during the deposition of the TPD.

Another cause of catastrophic failures in OLEDs is the crystallization of the organic materials. Since these have very low glass temperatures ($T_g \approx$ 80-100 °C), they readily crystallize during operation or during extended periods of storage, even in an inert atmosphere[38]. This problem can be addressed by using different materials, specifically high T_g polymers.

2.4.4 Long Term Wear-out

The EL output of an OLED will typically degrade exponentially while under bias[3,39]. Many possible mechanisms are thought to cause long term degradation, but the major contributor is believed to be due to impurities introduced during fabrication[36]. These impurities will enhance the concentration of carriers near them, resulting in exciton quenching, charge trapping, or catalysis of degradative reactions. Another contributing mechanism is the diffusion of TPD into the Alq_3 layer, where it may interact chemically and lead to quenching of some of the radiative excitons.

Reactions between the organic materials and the electrodes may result in degradation. Aziz *et al.*[40] have extensively studied the degradation process at the organic-cathode (Mg:Ag) interface. With the expected oxidation of the Mg in the cathode, they observed that there was a reaction between the Alq_3 and the Mg producing $Mg(OH)_2$ at the interface. This hydroxide was found to contribute to the formation of dark spots of two general forms: longitudinal structures with spherical endings at one end and elevated cathode bubbles.

2.5 Contacts and Surface Effects

2.5.1 The Work Function

The work function W of a metal is defined as the difference in potential energy of an electron between the vacuum level and the Fermi level. The vacuum level is the energy of an electron at rest at a point far enough away such that there are no electrostatic interactions between the metal and the electron. This is typically about 100 Å from the surface. The orientation of the exposed surface affects the value of the work function because the strength of the electric dipole layer at the surface depends on the concentration of surface positive ion cores. The dipole layer exists because the surface ions are in an asymmetrical environment, with the atmosphere to one side and the substrate on the other.

The work function is equal to the threshold energy for photoelectric emission at absolute zero. Therefore, using the Einstein relation one obtains the relationship[41]:

$$\hbar\omega = W + T, \tag{2.14}$$

where T is the kinetic energy of the emitted electron, W is the work function, and $\hbar\omega$ is the threshold energy. Work functions of materials used in this work are shown in Table 2.1.

Material	Energy (eV)
ITO	4.4-4.5 [42], 4.7 [43], 4.9 [22], 5.3 [44]
Pd	5.0[45]
TPD (HOMO)	5.53[22]
Alq_3 (LUMO)	3.05[22]
La	3.5[45]
Mg	3.66[45]
Ca	2.87[45]
Al	4.2[45]

Table 2.1: Fermi, HOMO, and LUMO energy levels for materials used in our OLEDs and some other commonly used cathode materials.

2.5.2 Ohmic Contacts

Ohmic contacts refer to a metal-semiconductor interface which is non-injecting and has linear current-voltage characteristics. The contact is acceptable if it can supply the required current density with a voltage drop that is very small compared to the drop across the active region of the device.

While the amount of literature available on ohmic contacts to inorganic semiconductors is vast[46], there is very little available on ohmic contacts to organic materials, although the same principles apply. Figure 2.7 shows a typical metal-semiconductor junction. The Fermi level of the metal will align with the Fermi level of the semiconductor and a depletion layer forms in the semiconductor.

In an ohmic junction, either the conduction or valence band of the semiconductor bends such that it is at the same energy level as the Fermi level in the metal. In the case of a *p*-type semiconductor making contact with a metal, the valence band is bent. This provides a low resistance interface between the two and for easy injection of holes into either material, depending if the device is operated under forward or reverse bias. For our case, the ohmic contact was made between the anode and the HTL. The Fermi level of the metal anode, ITO or Pd, should be well matched to the HOMO band of the HTL. As shown in Table 2.1, the energies of the anode Fermi level and the HTL HOMO band are very similar.

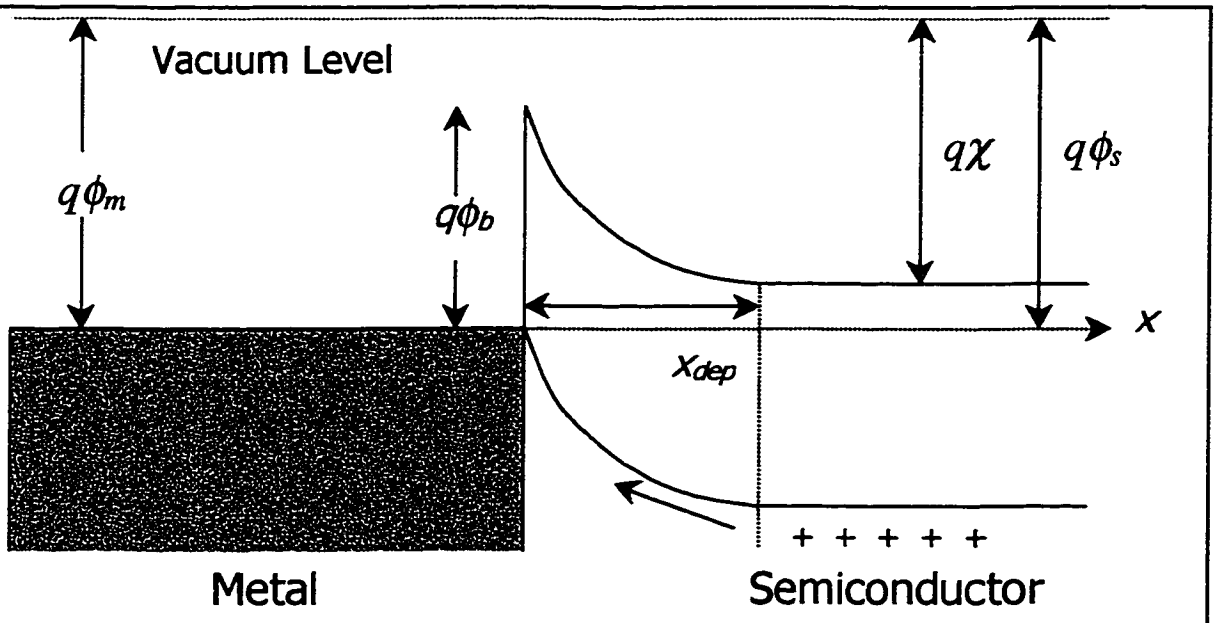

Figure 2.7: Energy diagram for an ohmic metal-*p*-type semiconductor contact.

2.5.3 Schottky Contacts

Metal-semiconductor contacts can be traced back to the work by Braun in 1874. In 1938, Schottky and Mott[47] suggested a model for this rectification mechanism using drift and diffusion concepts. There have been several reviews of metal-semiconductor contacts[48]. Figure 2.8 shows the energy diagram for a Schottky contact between a metal and an *n*-type semiconductor.

This is a high resistance junction. Injected electrons must overcome the barrier height $q\phi_b$. The Schottky-Mott equation can be written as: [47]

$$V = q\phi_{bo} = q\phi_m - q\chi\,, \tag{2.15}$$

where ϕ_{bo} is the contact barrier height, ϕ_m is the metal work function, and χ is the electron affinity of the semiconductor. Again, in the case of the Alq_3-cathode junction, the LUMO band values and the Fermi level of the cathode are similar (see Table 2.1) thus minimizing the energy barrier that the injected carriers must overcome.

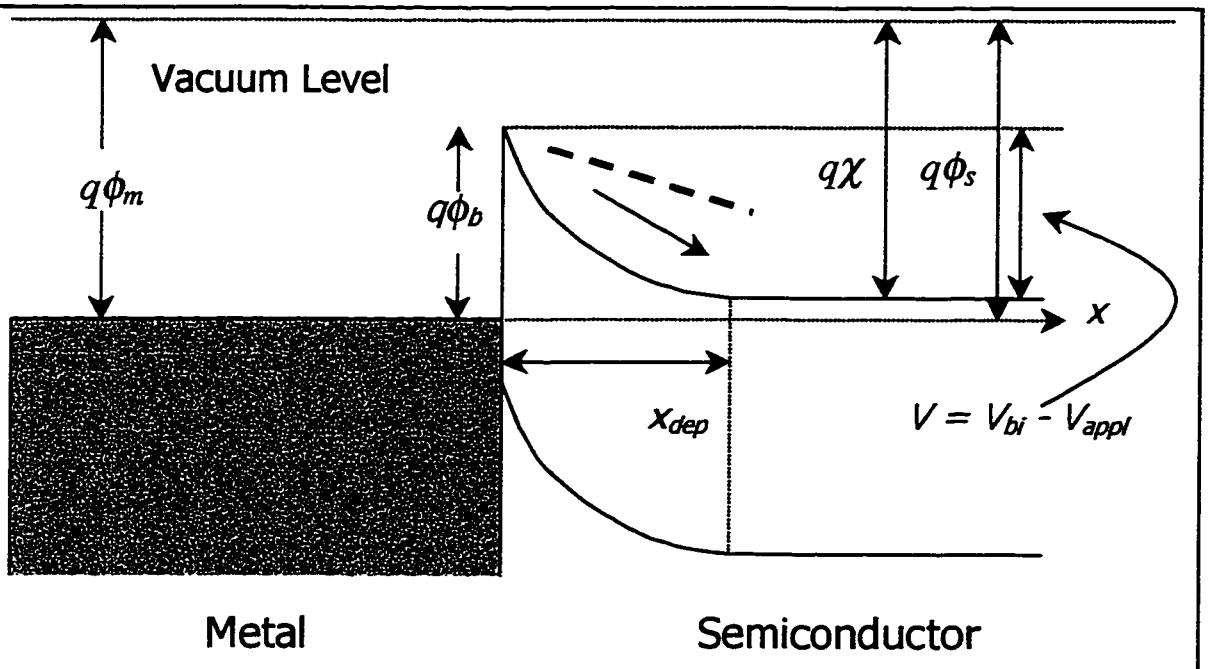

Figure 2.8: Energy diagram for a Schottky for a metal-*n*-type semiconductor contact.

2.6 Materials

2.6.1 Organic Materials

2.6.1.1 Hole Transport Materials

Since the advent of OLEDs, it has been found both through in depth studies and by observation that the hole transport material must exhibit good thermal stability (i.e., a high glass temperature). Other important properties include a matched energy barrier between the HTM HOMO level and the Fermi level of the anode as well as the ability to form a smooth continuous film on top of the anode.

There are many possible hole transport materials available, most of which were originally developed for xerography and are arylamine derivatives[49]. Of these derivatives, it was found that those belonging to the tri-arylamine family, to which TPD is a member, are the most useful as hole transport materials.

The PL peak is centered at approximately 420 nm with a full width at half maximum of approximately 60 nm. The hole mobility is estimated to be in the order of 10^{-3} cm^2/Vs [50]. The electron affinity and ionization potential are 2.4 eV[22] and 5.5 eV[22], respectively.

2.6.1.2 Electron Transport and Emitter Materials

Most electron transport materials are also used as emitters. In the case where a laser dye is used as the active material, the ETL must provide efficient transport and injection of charge from the cathode to the emitter if a separate dye layer is used, or provide efficient Förster energy transfer[6] if the dye is embedded within the ETL. While laser dyes have high fluorescent quantum efficiencies and are stable in air, the fluorescence efficiency of most of these dyes is strongly dependent on their concentration. If the concentration is too high, a phenomenon known as self-quenching will occur and the output of the device is considerably decreased.

The most important electron transport materials are chelated metals. A chelate is a metal complex that contains coordinated ligands which are capable of occupying more than one coordinated position on a central metal ion in a complex. As previously mentioned, Alq_3 is used as the ETL and emitter material in all of the devices used in this work. Alq_3 has a peak emission of 530nm with a full width at half maximum of approximately 108 nm. Its photoluminescence quantum efficiency (solution) is about 11% [51] and thin film room temperature PL quantum efficiency is approximately 32%[52] independent of film thickness over the range 10 nm to 1350 nm. Electron mobility is

estimated to be around 10^{-5} $cm^2/V \cdot s$ [53]. The electron affinity and the ionization potential are 3.05 eV[22] and 5.8 eV[22] respectively.

Unlike TPD, Alq_3 has a relatively high glass temperature (175 °C) and it tends to form a very good film when sublimed. Alq_3 can also be considered as a metallized pigment, which is more stable than a pure dye. Furthermore, it is also an organometallic which mediates the transition from a metal electrode to a pure organic (HTL).

2.6.2 Electrode Materials

2.6.2.1 Indium Tin Oxide

ITO has the unique property of being a transparent conducting material when in thin film form. It is formed by the substitution of the In^{3+} by Sn from the cubic bixbyte structure of indium oxide[54]. The conduction band of ITO consists of mainly indium and tin 5s orbitals while the valence band is dominated by oxygen 2p orbitals[55]. The stoichiometry, which can be typically written as $In_{2-x}Sn_xO_{3-2x}$, and physical properties of the ITO system are very much dependent on the deposition technique used, pre- and post-processing treatments (see Table 2.2). The lattice parameter of ITO is similar to that of In_2O_3 and lies in the range 10.12 to 10.31 Å[56].

Studies of ITO films grown by r.f. sputtering at room temperature on a glass substrate indicate that the ITO film has amorphous characteristics[57]. It has been shown that a temperature increase to approximately 200°C will lead to a polycrystalline structure and annealing will result in near single crystallinity with uniform grain size resulting in increased conductivity. It has also been suggested that deposition of ITO on single crystal substrates rather than amorphous glass can enhance the grain growth process[58].

Deposition Technique	Thickness [Å]	Carriers N [cm^{-3}]	Resistivity ρ [Ω·cm]	Transmittance [%]	Ref. No.
r.f. Sputtering	7000	6×10^{20}	3×10^{-4}	90	57
r.f. Sputtering	5000	12×10^{20}	4×10^{-4}	95	59
r.f. Sputtering	4000	3×10^{20}	8×10^{-4}	-	60
Magnetron Sputtering	800	6×10^{20}	4×10^{-4}	85	60
d.c. Sputtering	1000	9×10^{20}	2×10^{-4}	85	61
Reactive Evaporation	2500	5×10^{20}	4×10^{-4}	91	62
Ion Beam Sputtering	600	2×10^{20}	12×10^{-4}	-	63
Spray Pyrolysis	3000	5×10^{20}	3×10^{-4}	85	64

Table 2.2: Typical electrical and optical properties of ITO deposited by various techniques.

2.6.2.2 Palladium

Palladium is a member of the platinum group of metals. It is silvery white in colour and is malleable and ductile. In crystalline form, it has an FCC structure. Palladium can also absorb up to 900 times its volume in hydrogen. Its melting point is 1554 °C. A commercial tungsten filament was used to evaporate a fine wire of palladium. The purity of the wire was unknown, but suspected to be low.

The complex refractive index of a palladium thin film[65] is shown in Figure 2.9. We can perform a linear fit to the refractive index data in the wavelength range $\lambda = 400$ to 600 nm and extract n and k for a wavelength of 550 nm (the emission wavelength of our devices). We find that:

$$n = 0.200 + 2.472\times10^{-4}\lambda, \tag{2.14}$$

$$k = 0.347 + 6.286\times10^{-4}\lambda, \tag{2.15}$$

and

$$N = n + ik. \tag{2.16}$$

Using equations (2.14) and (2.15), the complex index of refraction for this region can be written as:

$$N = 1.56 + 3.80i, \tag{2.17}$$

Applying the transfer matrix method[66], but using the film thickness as the variable parameter, we can find the transmission of light at the emission wavelength, which is shown in Figure 2.10. Therefore, we see that there is a strong dependence of transmission on film thickness, so the film must be designed to balance the transmission of light versus the resistivity and continuity of the film.

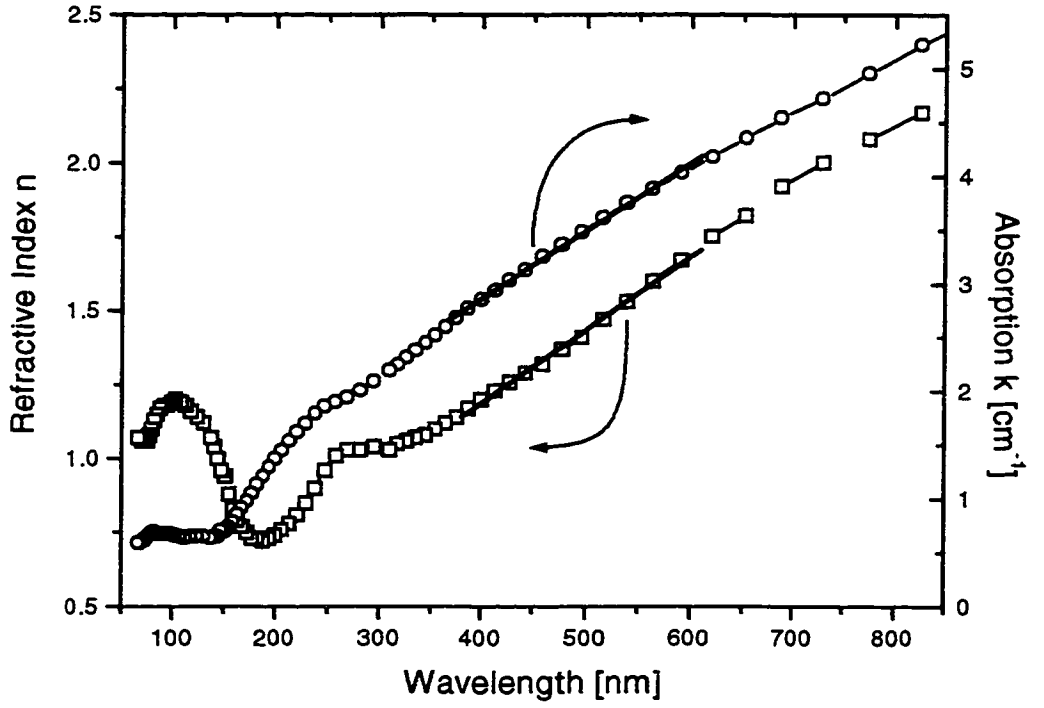

Figure 2.9: Index of refraction n and absorption coefficient k for palladium (after reference 65).

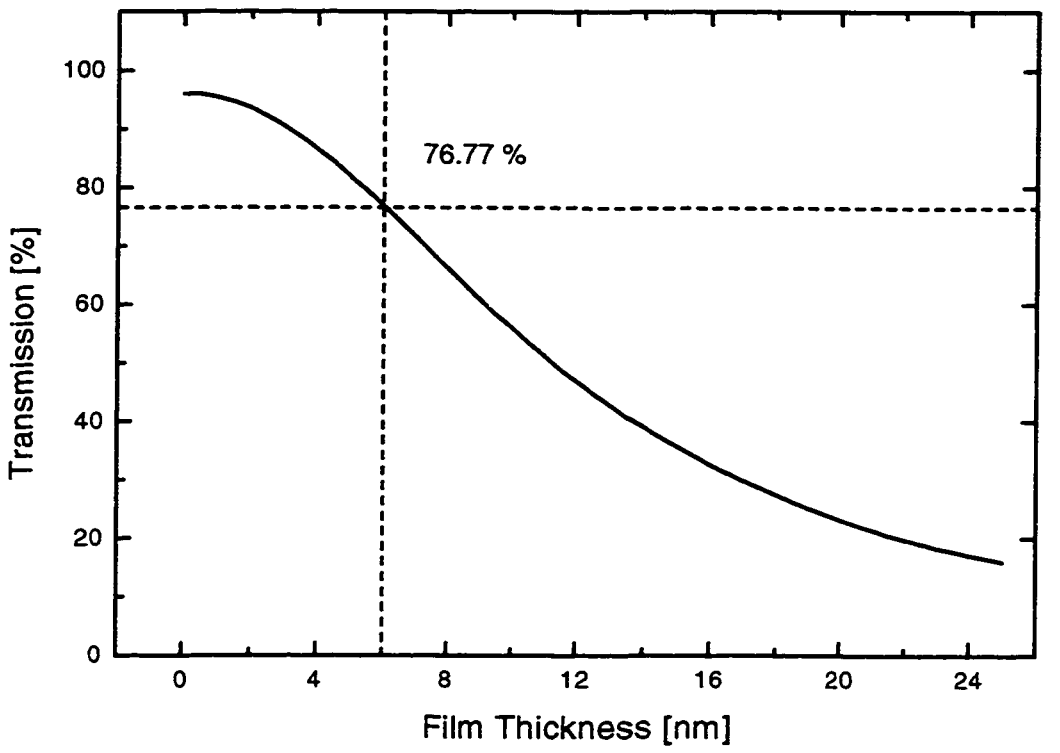

Figure 2.10: Transmission of a palladium thin film as a function of the film thickness for light at 530 nm. At 6 nm, the film has a transmission of almost 77%.

2.6.2.3 Lanthanum

Lanthanum is one of the most reactive of the scandium sub-group of elements. It is a soft ductile white metal which rapidly oxidizes when exposed to air and reacts with water to produce hydrogen gas. Lanthanum forms a hexagonal close packed / FCC crystal structure. Its melting point is 921 °C. Lanthanum was cut from a boule and a metal brush was used to remove as much lanthanum oxide as possible from the surface. The chips were then shaped into conical pieces to allow easy placement within the tungsten filament. The lanthanum boule was stored in a dry nitrogen environment to minimize oxidation. However, despite the removal of oxide on the outer surface, there was a

substantial amount of oxide present within the boule. Due to the oxide's similar melting point and vapour pressure, it was evolved simultaneously with the lanthanum.

2.6.2.4 Yttrium

Yttrium, like lanthanum, is a member of the scandium sub-group of elements. Unlike lanthanum, yttrium is relatively stable in air, but it will burn easily and will react with water to form hydrogen gas. Yttrium also forms a hexagonal close packed / FCC crystal structure with a melting point of 1522 °C. Yttrium shots were shaped into conical pieces to allow easy placement within the tungsten filament underneath the lanthanum pieces. Yttrium oxide was removed from the surface with a metal brush prior to placement in the deposition system.

2.6.2.5 Silver

Silver is a soft malleable metal with a characteristic sheen. It has the highest thermal and electrical conductivities of all the metals. It is stable in air and water, but is attacked by sulphur which produces a black layer of silver sulfide. Silver forms an FCC crystal structure and has a melting point of 961.9 °C. Silver shots were placed in a molybdenum boat without any prior treatment. The purity was greater than 99.99%.

3. Experimental Techniques

3.1 Substrate Preparation

All substrate preparation, device fabrication, and characterization were carried out in clean rooms with ratings of 50,000 and 10,000 particles over 1 μm in diameter per cubic foot of air. OLED devices were fabricated on glass slides that have been either pre-coated with ITO or onto palladium thermally evaporated in-house. The pre-coated glass slides were obtained from the Institut National de la Recherche Scientifique (INRS) Énergie et Matériaux research center, as well as the Thin Films group from the Institute for National Measurement Standards (INMS) at NRC. The thickness of the commercial ITO layer was 85-120 nm (60 nm for INMS ITO) with a surface resistivity of 30 Ω/□ and a resistance of 2.6×10^{-4} Ω cm. The thickness of the palladium films was typically 6-8nm with an unknown sheet resistivity and resistance.

The ITO slides were patterned and etched with 38% hydrochloric acid in a 1:1 acid-DI water solution for approximately 10 minutes. The slides were then cleaned with detergent and DI water, trichloroethylene, acetone and isopropyl alcohol in an ultrasonic cleaner with nitrogen drying between each step. Finally, the substrates were placed in a PR-100 UV ozone photoreactor (UVP Inc.) for 30 minutes immediately prior to placing

Material	Melting Point (°C)	Density (g/cm^3)	Temp. (°C) for $\approx 10^{-8}$ torr	Acoustic Impedance (10^5 cm^2 g^{-1} s^{-1})	Evaporation Technique
Pd	1554	12.0	842	36.1	W Coil
TPD	210	1.2	–	6.0	Mo Boat
Alq_3	320	1.4	–	6.0	Ta Boat
La	921	6.2	990	1.0	W Coil
Ag	962	10.5	847	16.7	Mo Boat
Y	1522	4.5	830	10.6	W Coil
La/Y	–	5.2*	–	10.0*	W Coil

* estimated values

Table 3.1: Physical properties of the evaporated materials.

the sample in the deposition chamber. The UV ozone process serves to passivate the ITO surface thereby reducing the possibility of short circuits in the device. For devices with a palladium anode, a glass substrate was cleaned using the process outlined above and loaded into the thermal evaporator.

Alq_3 was purchased from Eastman Kodak and Aldrich Chemicals while the tri-phenyl diamine derivative was purchased from H. W. Sands, both in powder form. With the exception of one device which used triply distilled Alq_3 from Aldrich, Alq_3 from Kodak was used as received while the TPD was doubly distilled. Vapour train sublimation was used to purify the organic materials.

3.2 Thermal Evaporation Chamber

3.2.1 Sample and Source Mounting

The clean substrate was then mounted on a chuck and placed in an Edwards 306 thermal evaporation chamber. The materials were placed into boats and mounted on a 4-source turret at the base of the chamber. TPD and silver were placed in dimple boats made from molybdenum while the Alq_3 was placed in a tantalum boat which was retrofitted with a lid which contained a pinhole in the middle to prevent the Alq_3 from spitting out of the boat as it was heated. It also served to define a more focused flux of molecules. Lanthanum and yttrium were placed in homemade braided tungsten filaments while palladium and aluminum were placed in a commercial tungsten coil.

Through trial and error, we found that using a 4-strand braid of tungsten wire (diameter 0.007") gave the best results. The braid was fashioned using a drill to twist the wires together until they formed a tight braid. A threaded brass piece was used as a template for the coil winding to ensure relative uniformity from coil to coil. The coil had

to be created to ensure that the heat transferred to the metal was maximized. In addition to this requirement, the ambient temperature had to be as low as possible and the coils had to be tight enough together so that minimal amounts of metal would drip out.

3.2.2 Thermal Evaporation Chamber

The base pressure of the Edwards chamber was 5.0×10^{-8} torr. This was achieved by using a combination of a scroll pump for roughing and a cryopump for fine pumping. Compared to other pumps, the cryopump offers several advantages such as pumping speed and oil-free operation. The Edwards deposition chamber is based on front door access as opposed to a bell jar. The chamber can accommodate four sources on the main turret and another three sources on posts at the rear of the chamber. The sources on the turret and posts are wired to allow them to be connected to either a 5, 10, or 30 volt power supply. A removable shield separated the sources on the turret serving to protect the organic materials from the high heat needed to evaporate some of the metals and also to minimize cross-contamination. In our depositions, only the sources on the turret were used.

The vertical throwing distance from the turret to the substrate was approximately 15-30 cm. For the deposition of the organic layers, the objective was to make a homogeneous film of each material. When the metals were being deposited, a shadow mask was placed a few millimeters in front of the substrate in order to pattern "fingers" onto the sample to provide several devices on one substrate (see Figure 3.1). The typical active area of the fingers was in the range 0.32 to 0.40 ± 0.02 cm^2.

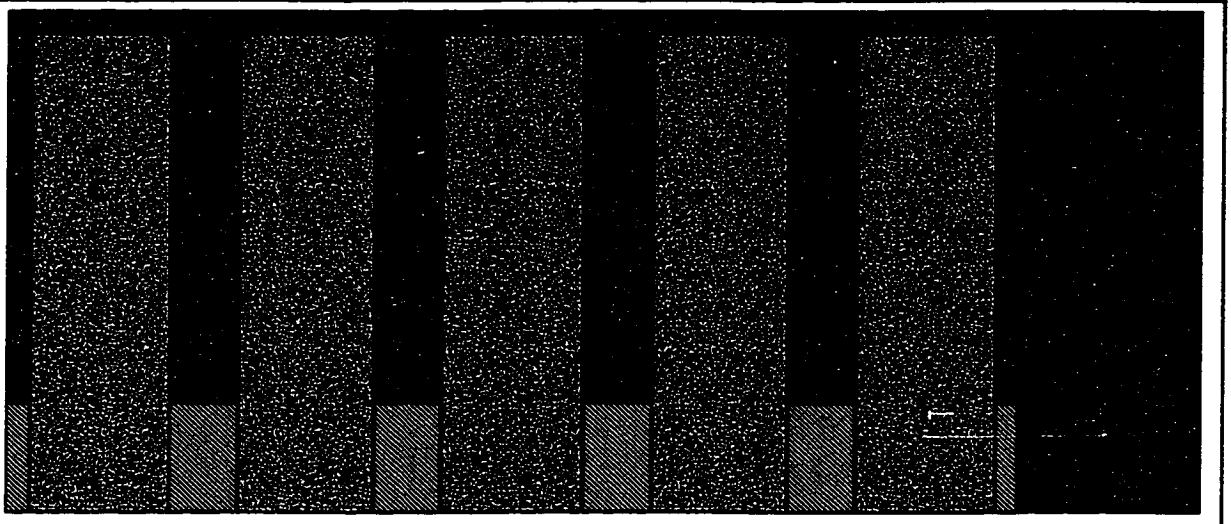

Figure 3.1: Top view of the OLEDs used. Section **a** has had ITO etched off while **b** has ITO. Both **a** and **b** are covered with the organic layers. Section **c** is the metal cathode which is on top of the organic layers. Contacts are made where part **c** overlaps part **a** and on part **b**. Light is emitted where section **c** overlaps section **b**. Diagram is not drawn to scale.

3.2.3 Device Fabrication

Typical deposition rates were of the order of 1-2 Å/sec for the organic materials. The deposition rates for the metals were slightly higher at 4-5 Å/sec as measured by a quartz thickness monitor placed beside the substrate. The thickness monitor operates by measuring the oscillating frequency of a quartz crystal. As material was deposited onto the crystal, the frequency decreased. By specifying the density and acoustic impedance of the material, the thickness of the deposited film could be calculated. The thickness monitor was also at a 20° angle from the vertical, thus a correction factor of cos(20) was introduced to compensate for the offset of the thickness monitor. The equation that is used to calculate the thickness is[67]:

$$T_{f=} = \frac{D_q}{D_f} \cdot \frac{N_q T Z_f}{\pi Z_q} \tan^{-1}\left[\frac{Z_q}{Z_f}\tan\left(\pi\left(1-\frac{T_q}{T}\right)\right)\right], \qquad (3.1)$$

where T_f is the film thickness, N_q is the frequency constant for the quartz crystal oscillating in thickness mode, D_q is the density of quartz, D_f is the density of the film, T is the period of the loaded crystal and T_q is the period of the unloaded crystal, Z_f is the acoustic impedance of the film material, and Z_q is the acoustic impedance of quartz.

The ambient temperature of the chamber at the substrate was measured by a K-type thermocouple. For the devices with pure lanthanum and lanthanum-yttrium cathodes, a thick layer of organic material (TPD or Alq_3) was deposited on top of the entire device to provide the cathode with some protection against oxygen and water penetration.

3.3 Characterization Techniques

3.3.1 I-L-V and EL Measurements

Current-luminance-voltage measurements were carried out simultaneously in the clean room. A Kepco DC power supply was used with a Hewlett Packard 3466A multimeter for voltage measurements and a Hewlett Packard 3458A multimeter was used for current measurements. A SpectraScan PR650 CCD camera fitted with a Macro-Spectra MS-75 lens controlled by a NRC 386 laptop computer was used for all spectral measurements (see Figure 3.2). EL measurements were performed when there was sufficient light emitted from the sample to provide a good signal to noise ratio. The analysis of I-V and XPS data was performed with Origin while the analysis of the AES data was performed with MatLab.

3.3.2 Other Measurements

Room temperature PL measurements were made using a 20 mW HeCd laser and a photo multiplier tube cooled to -18°C using a thermoelectric cooler. A filter with a cutoff wavelength of 455 nm was placed in the path of the collimated light beam when the spectrometer reached 455 nm to eliminate a very intense harmonic at 650 nm from the pump laser beam. The organic materials were in powder form, placed between two thin glass slides, sealed with teflon tape, and mounted vertically in a cryostat. A diagram of the apparatus is shown in Figure 3.3.

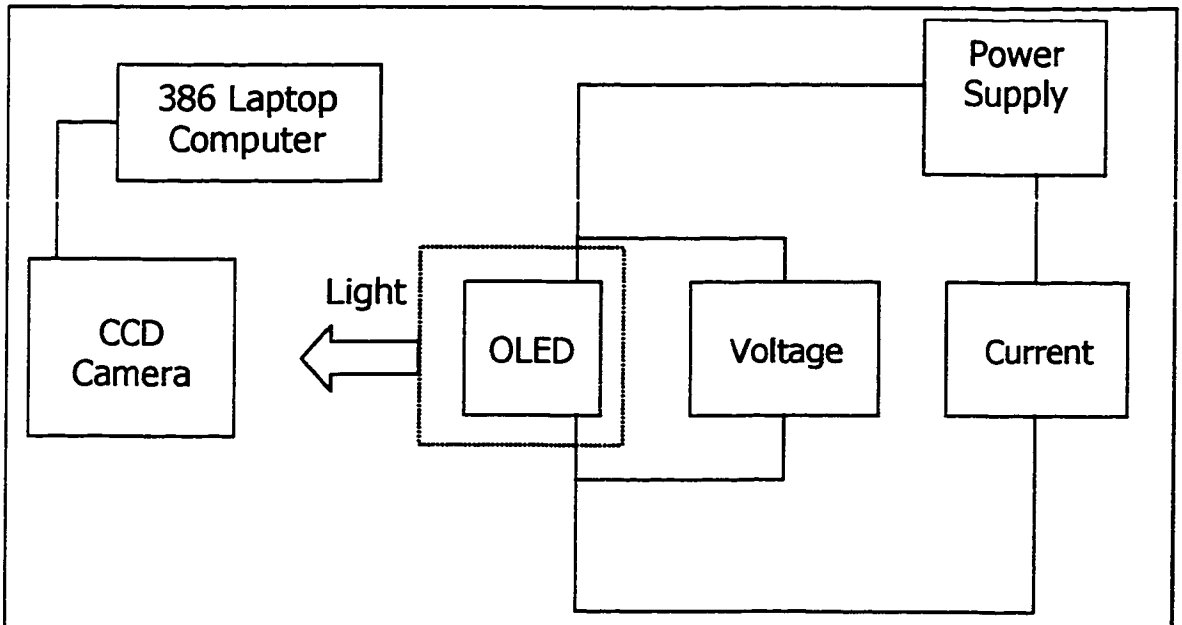

Figure 3.2: Schematic layout of the I-L-V and EL characterization apparatus.

Auger electron spectroscopy was performed by Irwin Sproule of the Surfaces and Interfaces Group at IMS using a Perkin-Elmer AES system. AES is based on the Auger radiationless process. When a core level of a surface atom is ionized by an electron beam, the atom may decay to a lower energy state through the rearrangement of electrons. This leaves the atom in a doubly ionized state. The energy difference between

these two states is given to the ejected Auger electron which will have a kinetic energy characteristic of the parent atom. The pressure of the system was approximately 10^{-10} torr and argon gas was used as the ion source. The ion gun was set to 5 keV with a spot size of 200x200 μm^2.

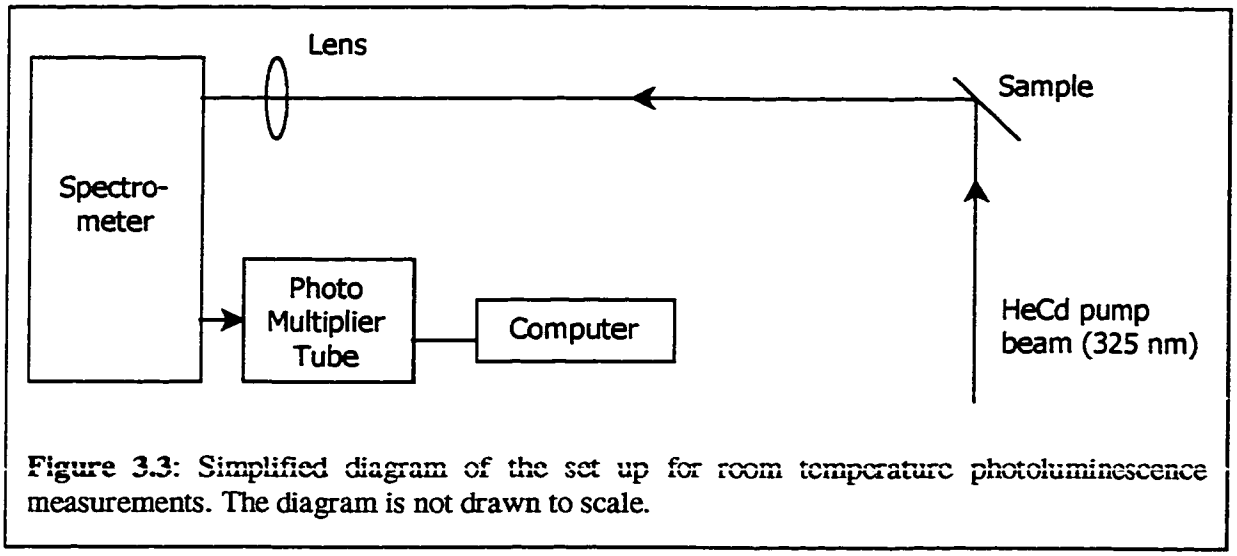

Figure 3.3: Simplified diagram of the set up for room temperature photoluminescence measurements. The diagram is not drawn to scale.

AFM imaging of the ITO on glass substrates was made by John McCaffrey of the Surfaces and Interfaces Group at IMS using a Digital Instruments Dimension 3000 AFM. X-ray photoelectron spectroscopy (XPS) was performed by Ye Tao of the Epitaxy Group at IMS using a Perkin-Elmer XPS system. The monochromatic x-ray source was obtained by using a graphite monochromator to isolate the aluminum Kα line at 1486.6 eV. The x-rays interact with the atoms in the surface region, causing electrons to be emitted via the photoelectric effect. Since each element has a unique set of binding energies, XPS can be used to identify and determine the type of elements and their concentration to a depth of several 10's of angstroms from the surface.

Scanning electron microscopy (SEM) and field emission scanning electron microscopy (FEM) was done by Jeff Fraser of the Surfaces and Interfaces Group at IMS

using a JEOL 840A SEM and a JEOL 6400F FEM. Scanning electron microscopy uses secondary electrons emitted from the sample to construct the image on the CRT. The electron source filament on the SEM is based on thermionic electron emission, which can be thought of as "boiling" the electrons off the filament. The FEM electron source filament is based on field assisted electron emission, which can be thought of as "pulling" the electrons off the filament. Field emission sources offer a lower energy spread of the electron beam, higher current densities and smaller source sizes. FEMs give ultra-high resolution and 500 to 1000 times brighter images than thermionic SEMs

4. Results and Discussion

4.1 Device Overview

We show in table 4.1 a summary of the devices which were fabricated as part of this work. NRC 222 was the only device which used the INRS ITO while NRC 240 had a 6nm thick layer of palladium.

Sample	Anode (nm)	TPD (nm)	Alq_3 (nm)	Cathode (nm)	Cap (nm)
NRC 236	ITO	60	60	La (60-65)	TPD (200)
NRC 237	ITO	60	60	La (200)	TPD (200)
NRC 240	Pd	60	60	La (120)	Alq_3 (200)
NRC 222	ITO	60	60	La (43)	Ag (100)
NRC 229	ITO	60	60	La (33)	Ag (100)
NRC 238	ITO	60	60	La (130)	Ag (200)
NRC 241	ITO	60	60	La/Y (80)	TPD (200)

Table 4.1. A summary of layer structure of the devices examined in this work.

4.2 ITO Anode Surface Morphology

The surface structure of the ITO is of critical importance in the performance of OLEDs. If it is rough, then the probability of shorts increases considerably.

In Figure 4.1a, we show an AFM image of ITO on a glass substrate that had undergone the full cleaning process, but had not been etched. The RMS roughness was measured to be approximately 1.25nm, which seemed surprisingly flat. The sample was then rotated by 90° and measured again. This allowed us to determine if the features in the original image were in fact real or system artifacts. According to Figure 4.1b, the RMS roughness is 1.44nm, confirming that the sample was very flat.

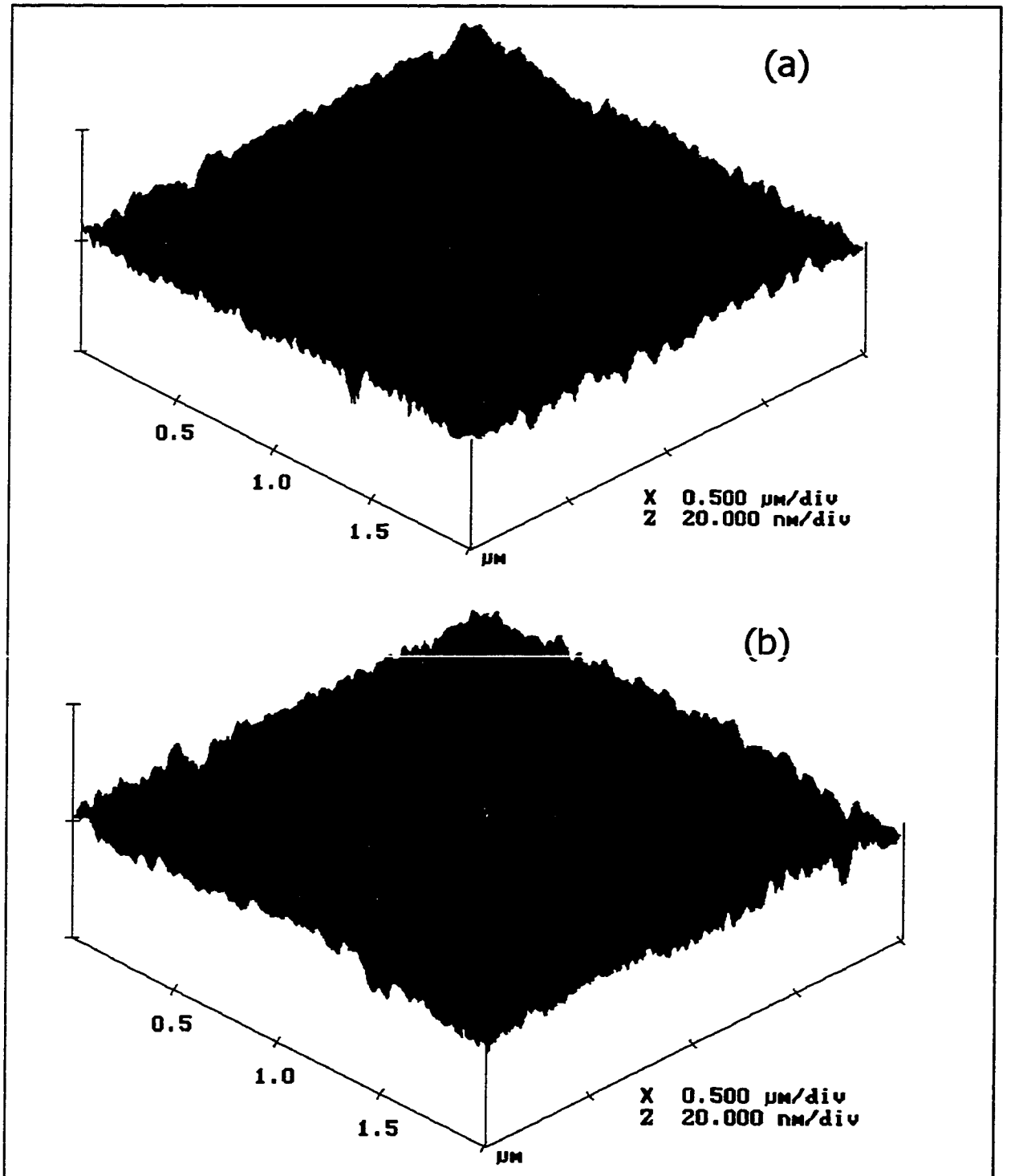

Figure 4.1: (a) An AFM image of an ITO on glass substrate that has not been etched but has undergone the standard cleaning procedure. The spot size is $2x2\mu m^2$ with a RMS roughness of 1.25nm. (b) The same sample rotated 90° to determine if there were any false surface features present. All measurement parameters were the same and the RMS roughness was found to be approximately 1.44nm.

Figure 4.2 shows another sample from the same set after it had been fully processed. The device fabricated on the ITO coated slide was then removed by soaking it in acetone and placing it in the ultrasonic cleaner for 20 minutes. The results for the same measurement procedure gives RMS roughness values of 1.47 nm for 0° (Figure 4.2a) and 1.26 nm for 90° (Figure 4.2b), which is surprising since the surface had been exposed to so many contaminants. Since these values are consistent before and after device fabrication, we can assume that the ITO samples are in fact very flat with an RMS roughness of approximately 1.3 nm. These measurements were only done on slides obtained from INMS (see Chapter 3).

We have seen that during etching in HCl, it is possible for the acid to seep underneath the photoresist and etch the protected ITO film, thereby eliminating that substrate for use in OLEDs. In Figure 4.3 we show an SEM of such a film.

4.3 ITO Anode & Lanthanum-based Cathodes

4.3.1 Lanthanum Cathode

Several devices using pure lanthanum were fabricated. The substrate was placed about 15 cm above the source thereby ensuring sufficient thickness of the layer. In Figure 4.4 we show typical current-luminance-voltage properties of one of these devices. As can be seen, light was detected by the CCD camera at an operating voltage of approximately 5 V with a nominal current density. The maximum luminance observed from this device was 1154 cd/m^2 at 16 V. This luminance value is about 11 times brighter than a standard CRT display and has an uncertainty of ± 4%.

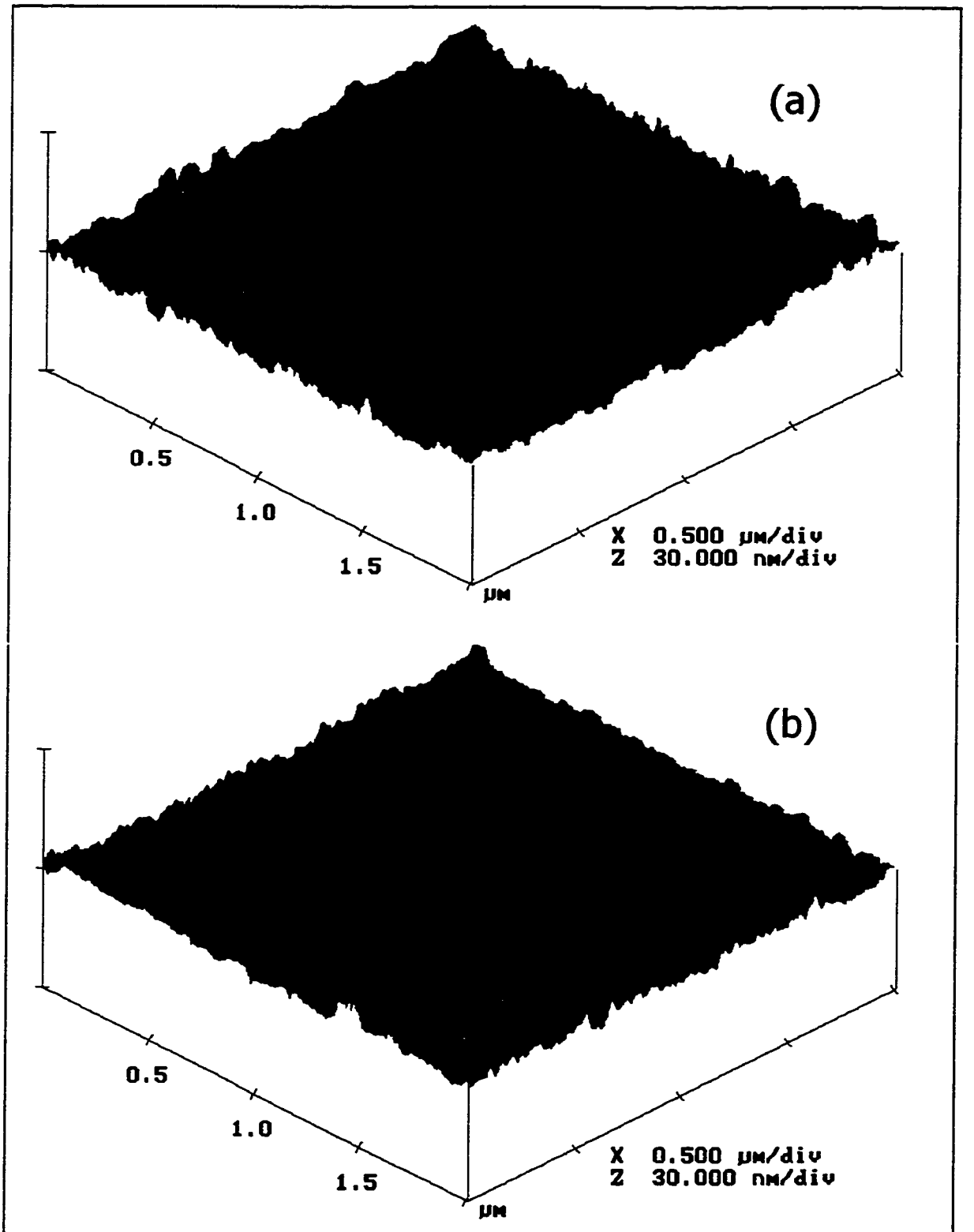

Figure 4.2: (a) An AFM image of an ITO on glass substrate that has had a device fabricated on it and removed. The spot size is $2x2\mu m^2$ with a RMS roughness of 1.47nm. (b) The same sample rotated 90° to determine if there were any false surface features present. All measurement parameters were the same and the RMS roughness was found to be approximately 1.26nm.

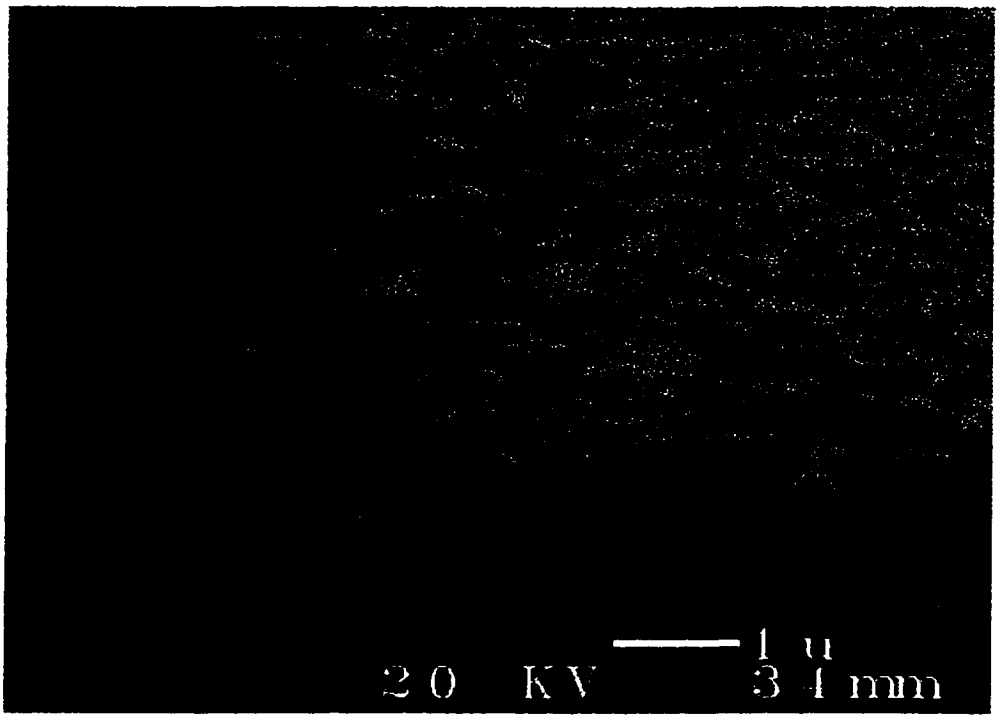

Figure 4.3: SEM image of and ITO on glass substrate that has had acid penetrate under the mask resulting in a rough ITO surface[68].

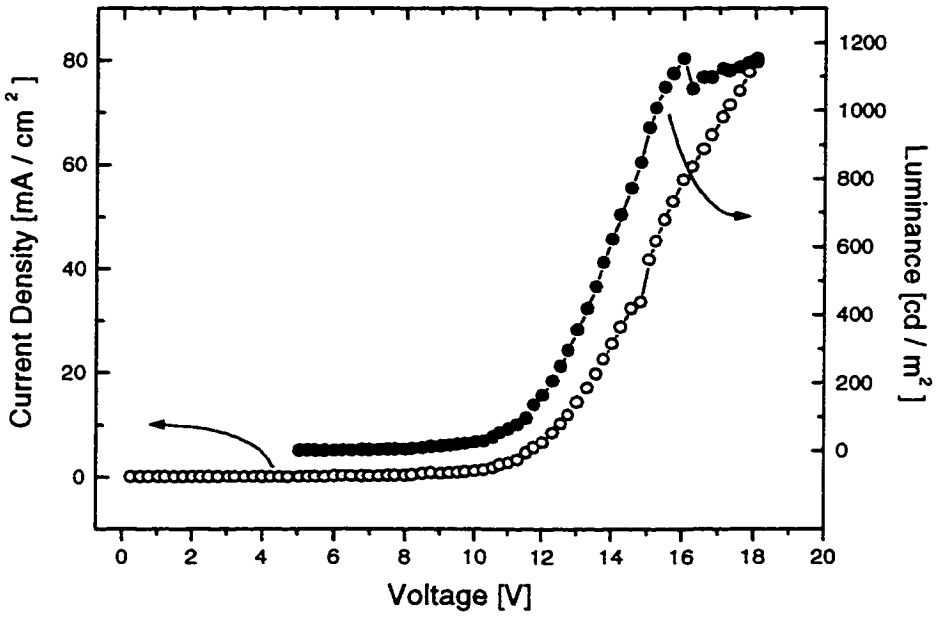

Figure 4.4: I-L-V characteristics for sample NRC 237.

The current measurements are subject to various sources of error. The major contributor is current fluctuation. Due to this instability, the integration time for each point is slightly different. For current readings at higher voltages, a small integration time is used since the reading is more stable. In this case, the reading is typically 5 to 20 milliamps while the drift is of the order of 100's of microamps. In the mid- and low-range voltages a larger integration time is used. Here the current drift tends to be very large compared to the current reading. The current readings are usually below 1 milliamp and the drift is anywhere from 10 to 100 microamps. Chemical reactions take place in the organic materials that alter the electrical properties and thus contribute to the current drift. These may include reactions between the two different organic layers, between the organic layer and the electrode, or other electrochemical reactions within one of the organic materials. However, as the voltage is increased, the current tends to become more stable, indicating that the device has reached chemical equilibrium. Taking into account measurable errors, the estimated errors are approximately the size of the data points.

For the remainder of this work, we will refer to the current density, J, rather than the current. This is done in order to facilitate the comparison of different devices. If we plot the current density versus voltage data on a log-log graph, as in Figure 4.5a, we can see the SCL regime has a slope of 2.2 ± 0.2 which is consistent with a V^2 relationship. The TCL regime is also visible and we can extract several parameters according to equation 2.5. We first determine that the trap energy levels are 0.18 ± 0.03 eV below the LUMO level, indicating the presence of deep traps. This result is consistent with the published values of Burrows *et. al.*[14] which quote trap energies of the order of 0.15 eV.

Furthermore, we can also extract the trap density, N_t, which was found to be about 10^{19} cm^{-3} with negligible error. This value is approximately one order of magnitude higher than the reported values by Burrows *et. al.*[14] indicating that there were impurities present in the Alq_3. The permittivity was also extracted from the fit, yielding a value of $1.7x10^{-12}$ F/m with negligible error.

If we take the same data and plot it according to a Fowler-Nordheim model (equation 2.8), as in Figure 4.5b, we can extract the barrier height at the ITO-TPD interface. Here we find that the barrier height $\phi = 0.11 \pm 0.02$ eV. While Fowler-Nordheim tunneling is the dominant mechanism in polymer-based devices[43], if it was dominant in our devices, we would observe a linear $\log(J/F^2)$ vs. $\log(F^{-1})$ graph.

However, we see that the data is linear only in the high field regime, indicating that a tunneling mechanism may be present. In the low field regime, the data deviates from a linear trend indicating the presence of some other mechanism.

Unfortunately, due to the high rate of oxidation of lanthanum, we were unable to perform any compositional analysis with AES due to charging effects. When AES is performed, the sample is kept at a constant bias. When there is charging of the sample, the potential of the sample will change, thereby shifting the energy spectrum. However, the time evolution of the J-V properties and SEM imaging were performed on the devices. In Figure 4.6, we show the J-V properties over a period of 1.5 hours. These measurements were performed at room temperature with approximately 40% relative humidity. As we can see, in as little as 60 minutes, the luminance of the device had almost degraded by a factor of three since no physical encapsulation of the device was used.

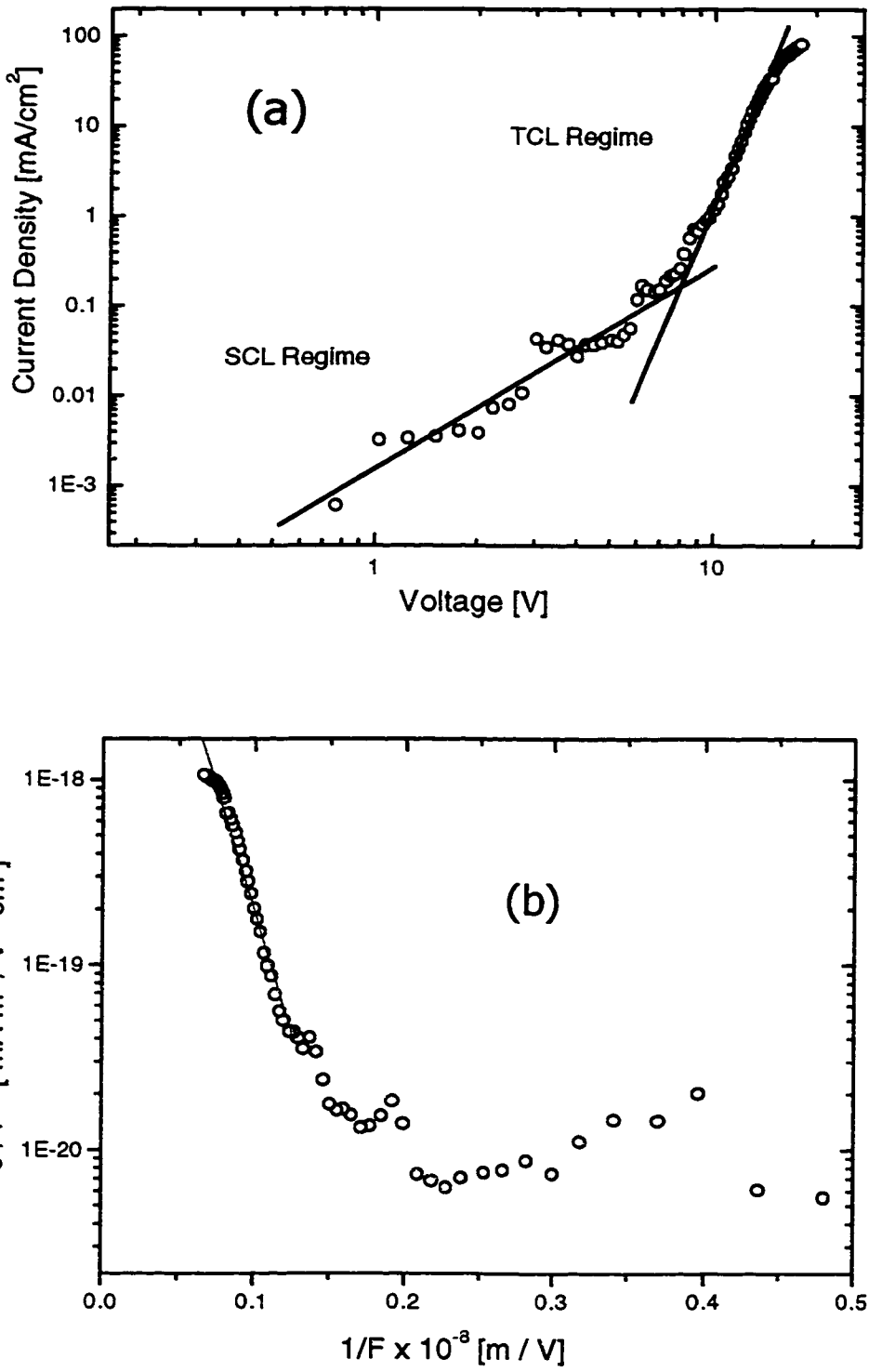

Figure 4.5. (a) log(J) vs. log(V). (b) A fit using the Fowler-Nordheim model.

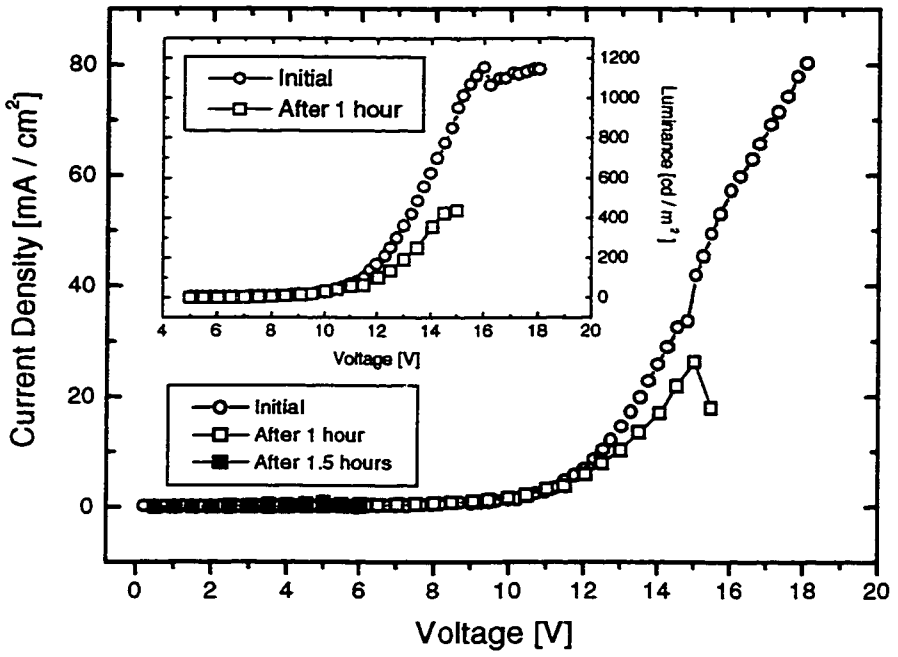

Figure 4.6. Time evolution of the J-L-V characteristics of an OLED with a lanthanum cathode.

An SEM image of sample NRC 236 is shown in Figure 4.7. This sample had a thinner lanthanum layer (~60 nm) and a 200 nm cap of TPD. We are uncertain if the flaking seen in Figure 4.7b is from the TPD or from the lanthanum. In Figure 4.8, we show the J-V characteristics for sample NRC 236. In this case, the cathode had completely oxidized before characterization could be completed. The range of data that was collected was consistent with the data obtained from sample NRC 237 in the same voltage range. Several other lanthanum-based devices were made, all of which exhibited similar results.

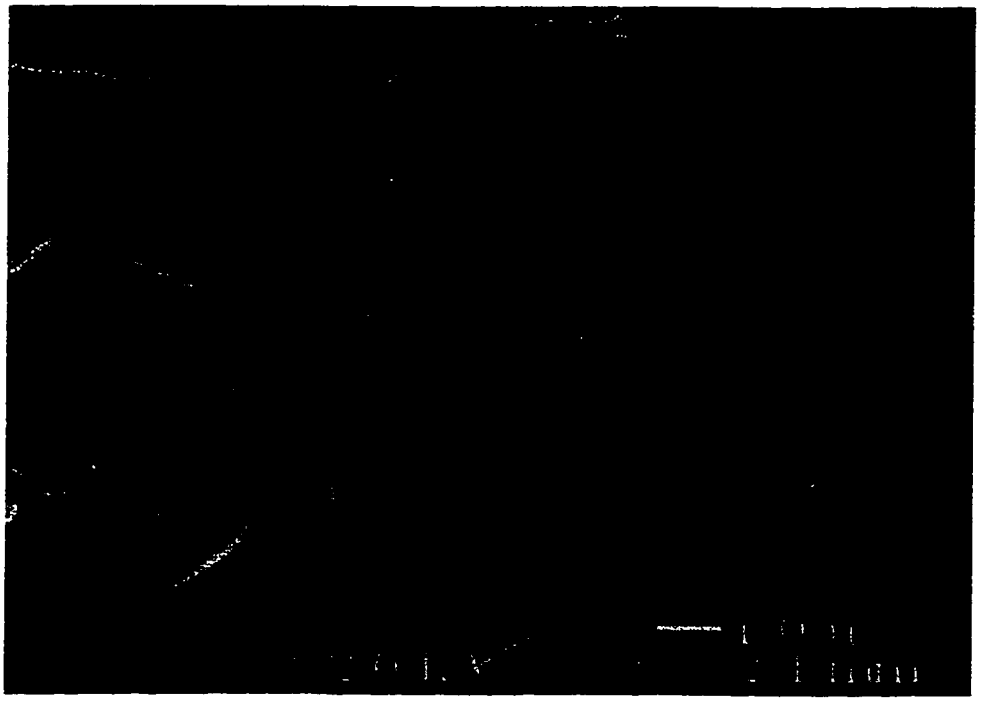

Figure 4.7: SEM of the surface of sample NRC 236 with a 60nm thick lanthanum cathode and a 200 nm thick TPD cap.

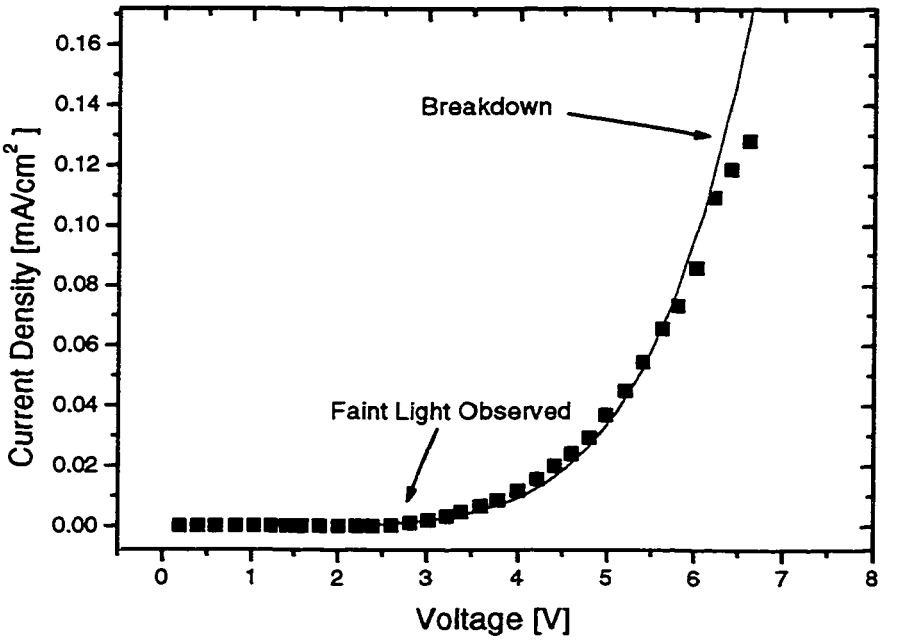

Figure 4.8: J-V characteristics for sample NRC 236. The thinner lanthanum layer caused pre-mature device failure. However, a fit to equation 2.3 gives good results.

4.3.2 Lanthanum-Silver Bilayer Cathode

Another common practice when dealing with a reactive cathode is to encapsulate it with another inert material. In this case, we chose silver as a capping material due to its superior electrical characteristics and its stability when exposed to water and air.

Sample NRC 222 is somewhat different from the other samples since the Alq_3 used had been triply distilled. This device was also fabricated with the sample approximately 30 cm above the sources and with larger shields to minimize the amount of cross contamination. Two sets of data will be shown to compare the effect of the Kodak Alq_3 and the triply distilled Alq_3.

Figure 4.9 shows the J-L-V characteristics of the first La-Ag bilayer device. The arrow indicates the region where initial shorts were burned out and the device entered its "normal" operating mode. The active area of this device was approximately 0.3 cm^2.

The vertical arrow in Figure 4.9 denotes where a massive short occurred in the device. Although this device only has one short, it is common for these devices to have many. Fitting this J-V data to equation 2.5 yields a trap energy $E_t = 0.16 \pm 0.01$eV and a trap density $N_t \approx 7\text{x}10^{18}$ cm^{-3} with minimal error.

In Figure 4.10 we show the J-L-V graphs for samples NRC 229 and NRC 238. We can see here that the J-V characteristics are very different from those of Figure 4.9. We believe the reason is due to cross contamination during growth as well as using Alq_3 of lower purity. When sample NRC 222 was grown, there were shields in place to isolate each source and to try to minimize cross contamination. For the latter two devices since the sample was lowered, these shields had to be removed. Due to this fact, the organic materials coated the turret electrode as they were being sublimed. When the metals were

deposited, they heated up the organic materials close to the source and evolved carbon along with the metal.

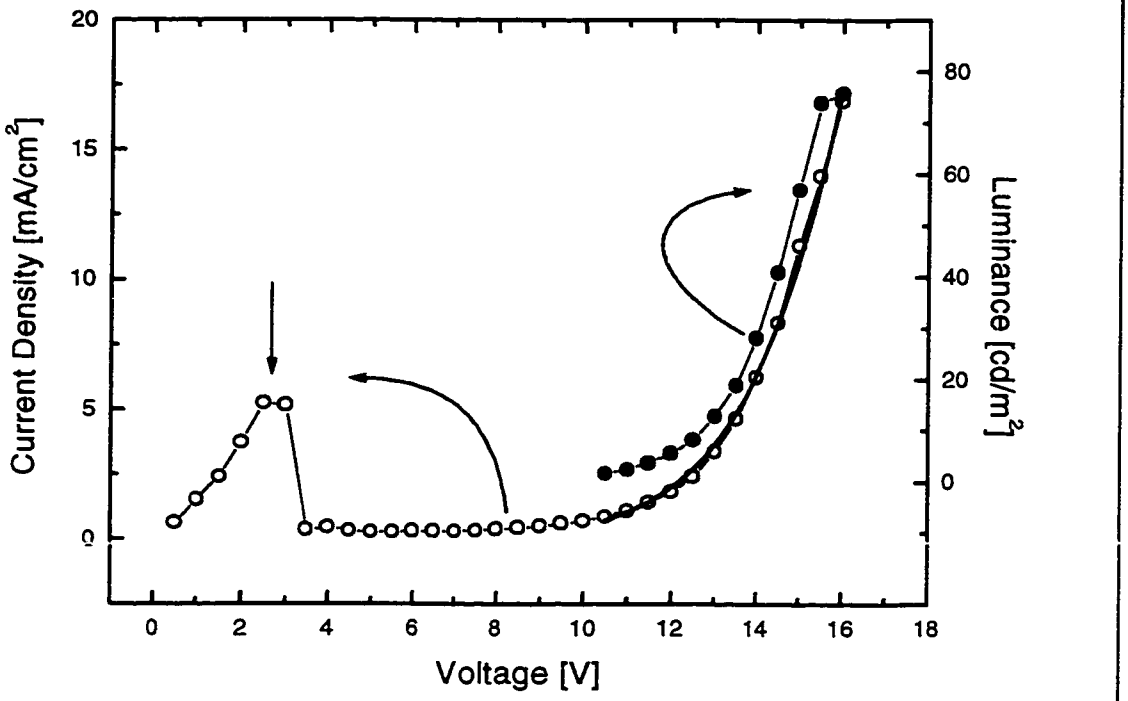

Figure 4.9: J-L-V characteristics for a La-Ag bilayer structure (sample NRC 222). The heavy line is a fit to equation 2.5 with $E_t = 0.16 \pm 0.01$ eV and $N_t \approx 7 \times 10^{18}$ cm^{-3}.

The J-V data in Figure 4.10 appears to be relatively linear throughout the entire voltage range, which indicates ohmic transport rather than TCL transport. If we perform a linear fit, we should be able to extract n_o using the literature value of μ_n[3,13,14] using equation 2.3. Here we find that n_o is of the order of 10^{20} cm^{-3}, which is unusually high compared to published[3,13,14] values of $\approx 10^{10}$ cm^{-3}. These values are very unreasonable for OLED devices, which leads us to the conclusion that the ohmic properties observed

were possibly due to the electrical properties of silver or the carbides which masked the diode I-V characteristics.

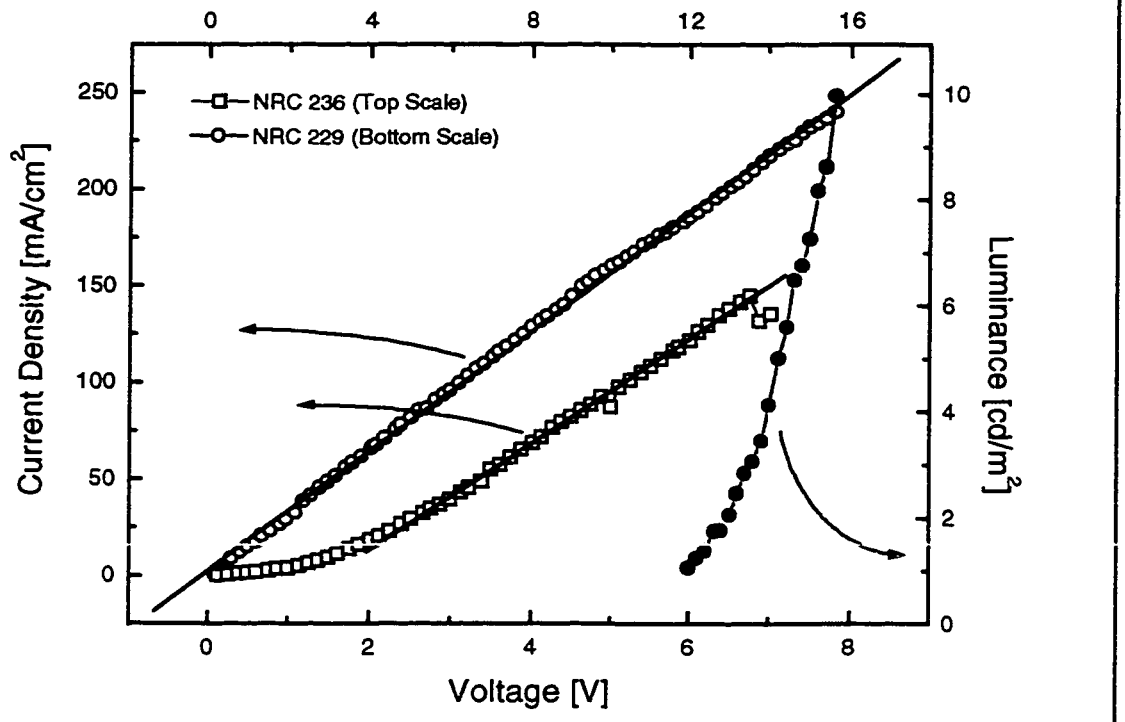

Figure 4.10: J-L-V characteristics for samples NRC 229 (O and •) and NRC 238 (□). No luminance values were measured from NRC 238. The low luminance values from NRC 229 are due to generally poor light output from the device as well as misalignment of the CDD camera with the sample.

In both of these devices, the light emission was very poor. When the device was in operation, the non-uniformity of the surface was visible to the unaided eye. There were dark patches all over the surface, indicating that perhaps the films were not homogeneous or that there was some contaminant present. This, combined with alignment problems with the CCD camera, contributed to the extremely low luminance values. We also note that the spectral information that was measured for this device was

done with the CCD's standard lens. The emitting area of the device took up approximately one quarter of the detector area. We can therefore say that the luminance values for this device was underestimated by at least a factor of four. These devices also drew considerably higher amounts of current, over 150 mA/cm^2 compared to less than 100 mA/cm^2 for the pure lanthanum and the first lanthanum-silver device (NRC 222). A possible explanation of this can be found in the AES data.

In Figure 4.11 we show the AES spectrum for sample NRC 222. In the main graph, we can see that the interface between the silver and lanthanum is very smooth. The organic layers are clearly visible between about 35 to 87 minutes with a distinct

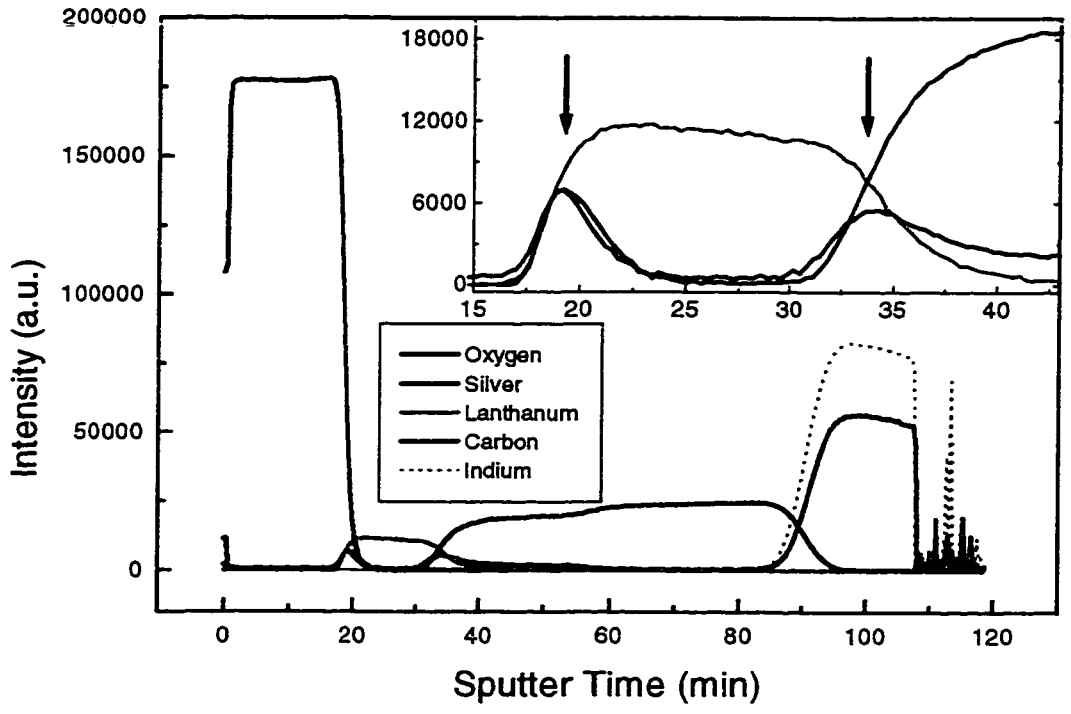

Figure 4.11: AES spectrum for sample NRC 222. After approximately 110 minutes, the glass substrate was reached. The inset shows an enlargement of the lanthanum portion of the device. Note the carbon and oxygen peaks on either side of the lanthanum layer.

intensity change at approximately 56 minutes, representative of the TPD-Alq_3 interface. If we look at the interface between the lanthanum and the Alq_3 layer, we can see that the lanthanum signal appears to penetrate quite far into the Alq_3. This is most likely due to the sputtering beam pushing the lanthanum atoms into the soft organic material. At the TPD-ITO interface we see that the carbon signal appears to be penetrating quite far into the ITO. This may be due to the organic materials "flowing" into the electron beam crater as sputtering occurs, creating a false carbon signal inside the ITO. The most interesting feature of this device is shown in the inset; the presence of a carbon peak at the La-Ag interface and oxygen peaks on either side of the lanthanum layer. In Figure 4.12 we show an elemental analysis of carbon and oxygen at several positions in the sample. It is clear that the carbon and oxygen spectra at the interfaces are different than those in the organic material, indicating carbide and oxide presence. In fact, we can see from the Alq_3-TPD interface that the oxygen content is steadily rising but a dramatic increase occurs near the lanthanum Alq_3 interface. This peak most likely has two contributing factors: a) oxygen in the Alq_3 layer reacting with the lanthanum to produce a thin layer of La_2O_3 at the interface and b) oxygen from the atmosphere may be able to travel down the interface between the layers. The other oxygen peak at approximately 20 minutes is most likely due to thermal oxidation of the lanthanum. At this point, the lanthanum source is usually almost empty and the rate of deposition drops from several angstroms per second to below 1.5 angstroms per second. This slowing of the rate and thermal currents generated from the silver source as it is being heated promotes thermal oxidation of the top-most layers of lanthanum in the device. The carbon peak also observed at 20 minutes is believed to arise from cross-contamination of the sources. It is

suspected that the carbon is evolved from the organic materials which previously coated the shields. Further analysis of this carbon peak showed that it had the same characteristic spectral shape as the carbons in the organic material. There may also be a

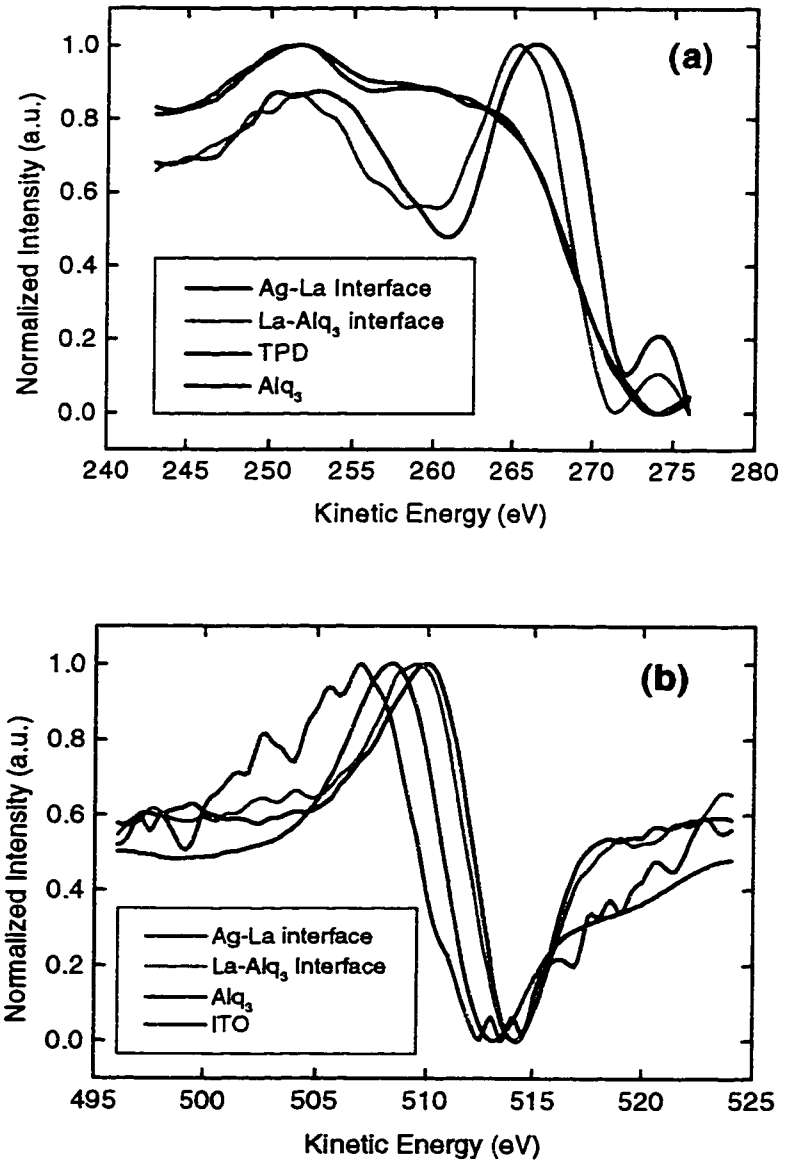

Figure 4.12: Carbon (a) and oxygen (b) elemental analysis taken at various places from sample NRC 222. From (a) is it obvious that the carbon spectra within the two organic materials are almost identical while on either side of the La cathode it has a carbide shape. Similarly in (b) the oxygen shape on either side of the La indicates the presence of an oxide.

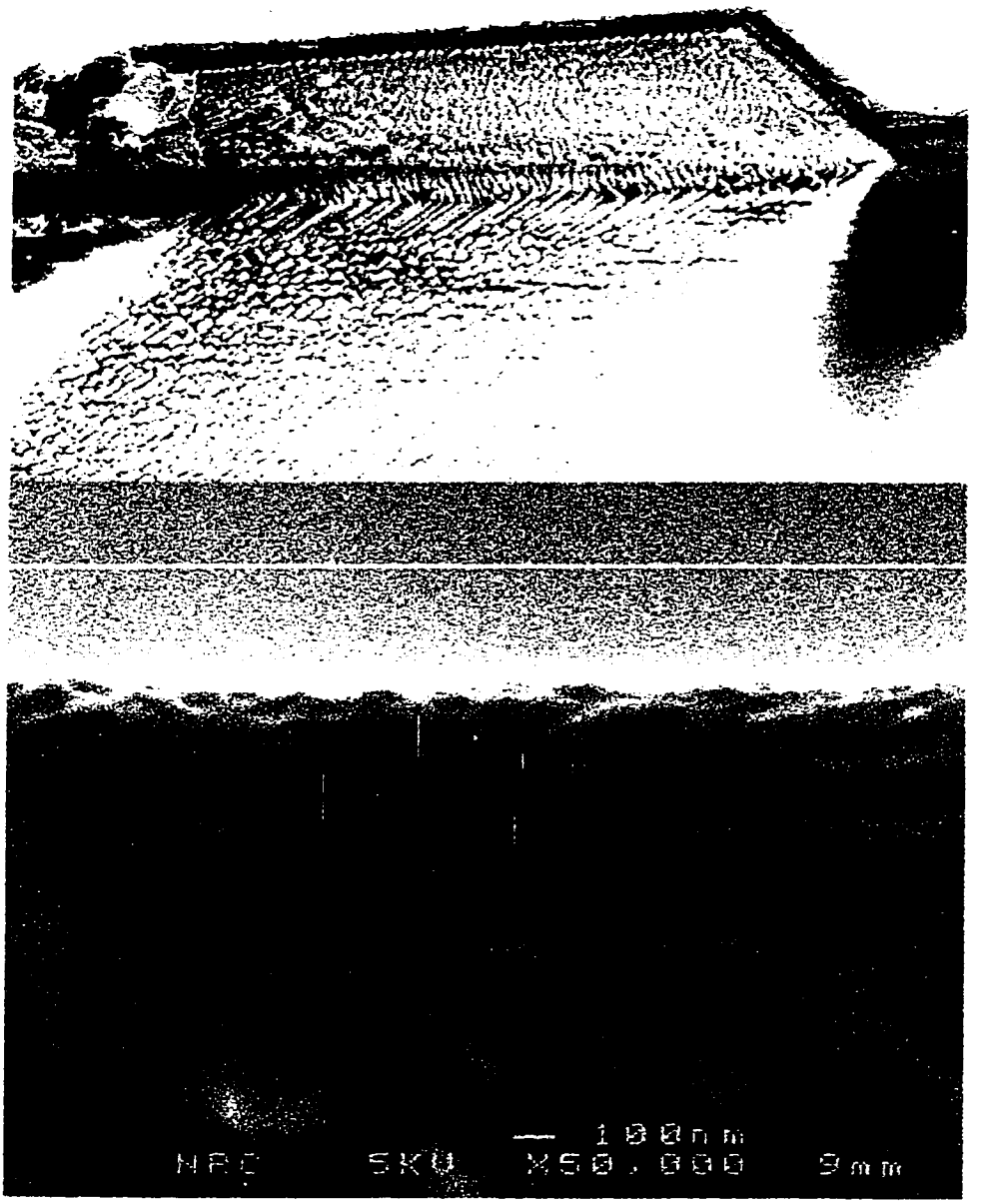

Figure 4.13: FEM cross-sectional image of sample NRC 222. In (a) we see the crater with the buckling of deposited layers on the left front corner. (b) shows the individual deposited layers with the exception of the organic layers, which appear as a dark band (orgs). The carbide and oxide layers are beyond the resolution of this imaging technique.

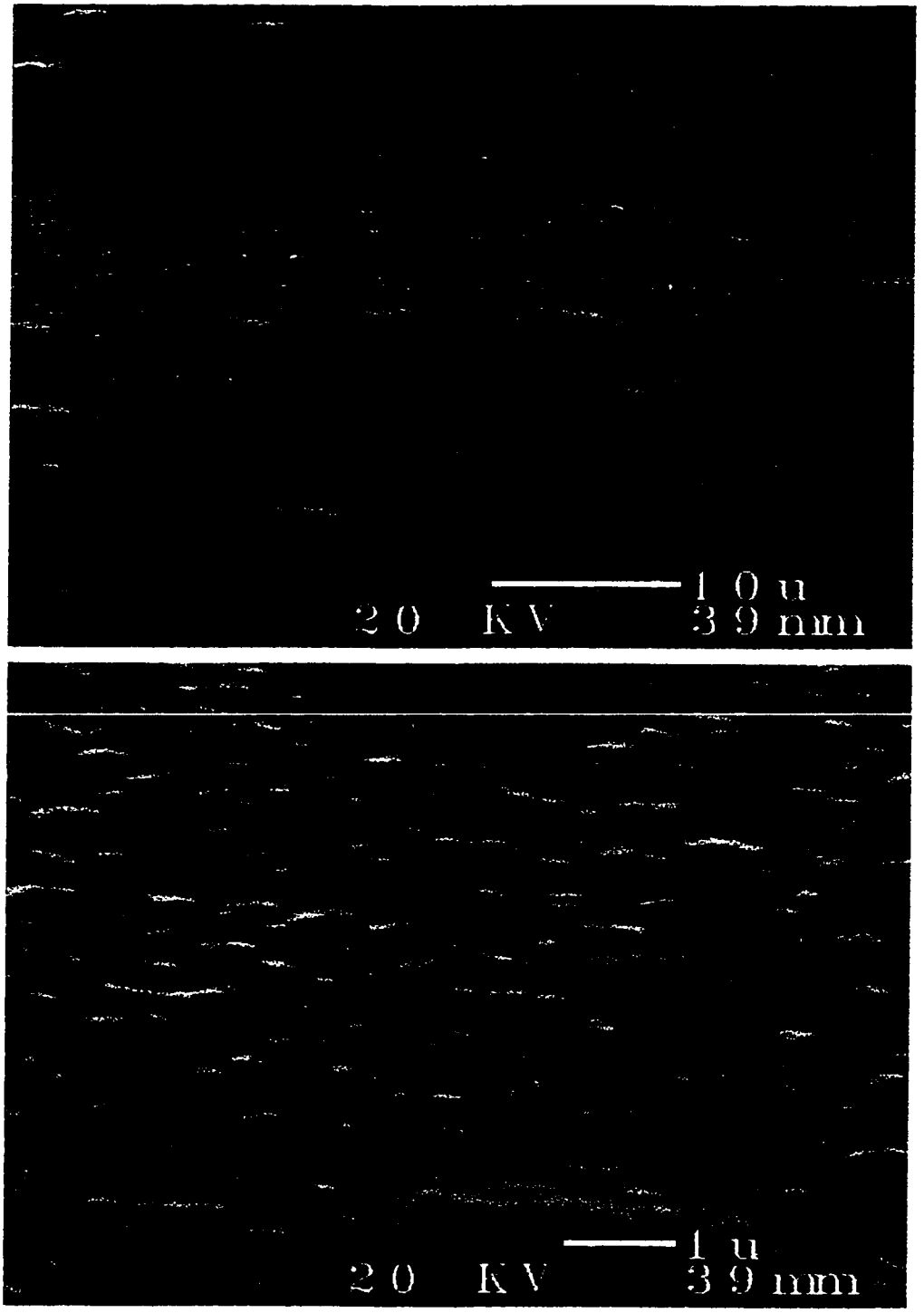

Figure 4.14: SEM images of the bottom of the AES sputtering crater in sample NRC 222. The lower image is a magnified portion of the upper image. We can see that there is a fair amount of blistering at the bottom of the crater. The black spot in the upper right corner of the top image is a portion where the sputtering rate was vastly different than the surrounding material.

carbon peak at the lanthanum-Alq_3 interface, but we were not able to distinguish it from the organic carbon signature.

The thicknesses measured from the FEM image are very similar to the thickness values reported by the *in situ* thickness monitor; 125nm total organic material (60 nm Alq_3 and 60 nm TPD target), 44 nm La (43 nm target) and 106 nm Ag (100 nm target).

We can also assume that this oxidation pattern is similar in the pure lanthanum cathode devices. In fact, this "natural" lanthanum oxide layer at the cathode-organic interface may be acting to create a metal-insulator-semiconductor (MIS) type structure. When a thin layer of insulating material is inserted between the metal contact and a semiconductor, the injection efficiency is greatly increased. This may also contribute to the low current densities observed with pure lanthanum devices.

If we compare Figure 4.11 to the AES spectrum for NRC 238 (Figure 4.15), the carbide peaks are more obvious. We hypothesize that the carbide appears in all of the silver-lanthanum devices after NRC 222 because the sample was brought closer to the sources, which exposed it to higher temperatures. Compositional analysis of oxygen and carbon, shown in Figure 4.16, was performed at several points in the device to confirm that we were observing oxide and carbide formation.

FEM imaging was also performed on this sample. For both NRC 222 and 238, the sample was cleaved and the ion mill from the SIMS characterization was used to bore a hole at the edge of the device.

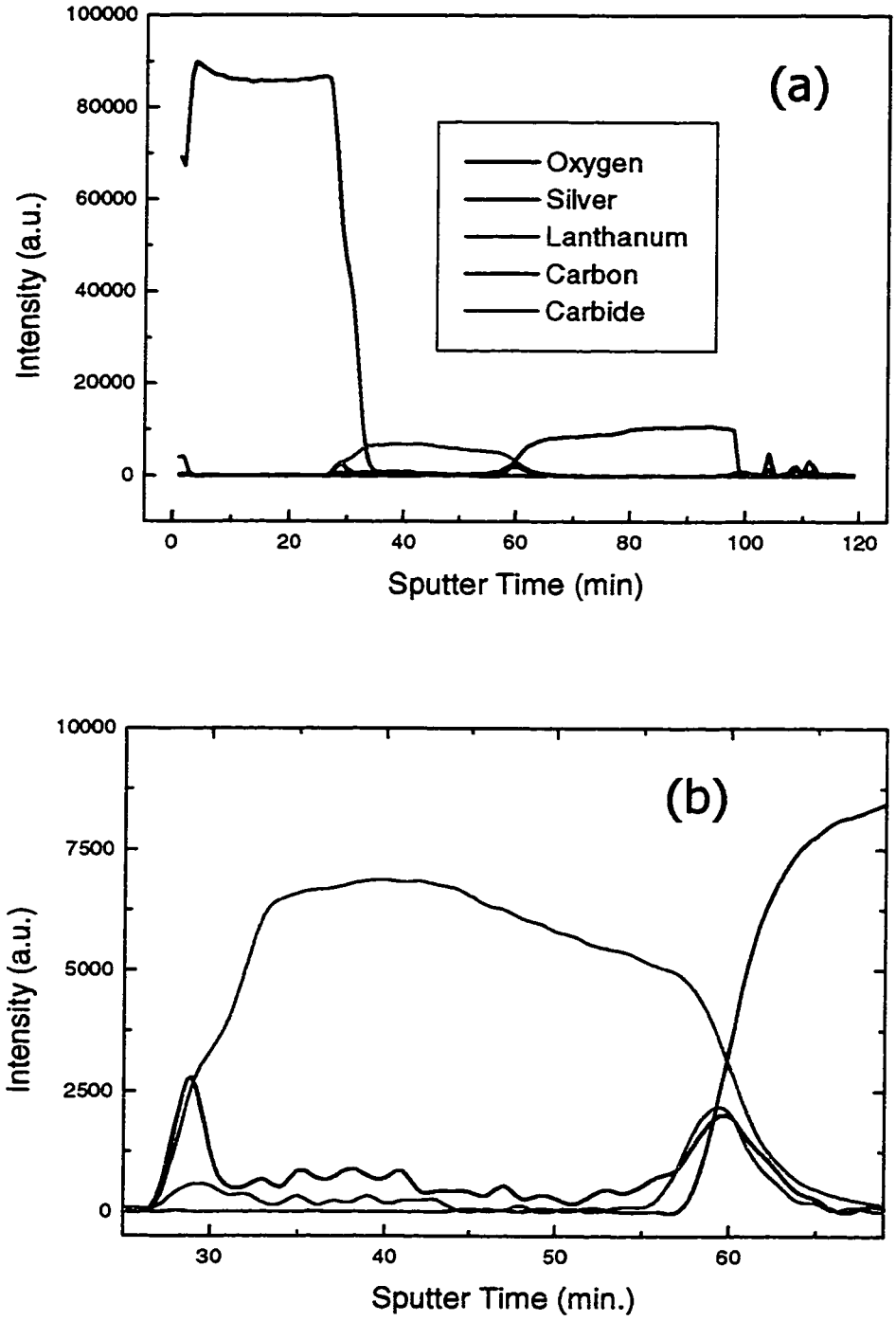

Figure 4.15: AES spectrum of sample NRC 238. (a) Shows the spectrum for the entire device while (b) is an enlarged portion of the La interface. We can see here that there are two different types of carbon signals present: one from the organic material and one from a carbide structure. The carbide peak is strongest at the La-Alq_3 interface and relatively weak at the La-Ag interface. Oxide peaks appear on either side of the lanthanum layer.

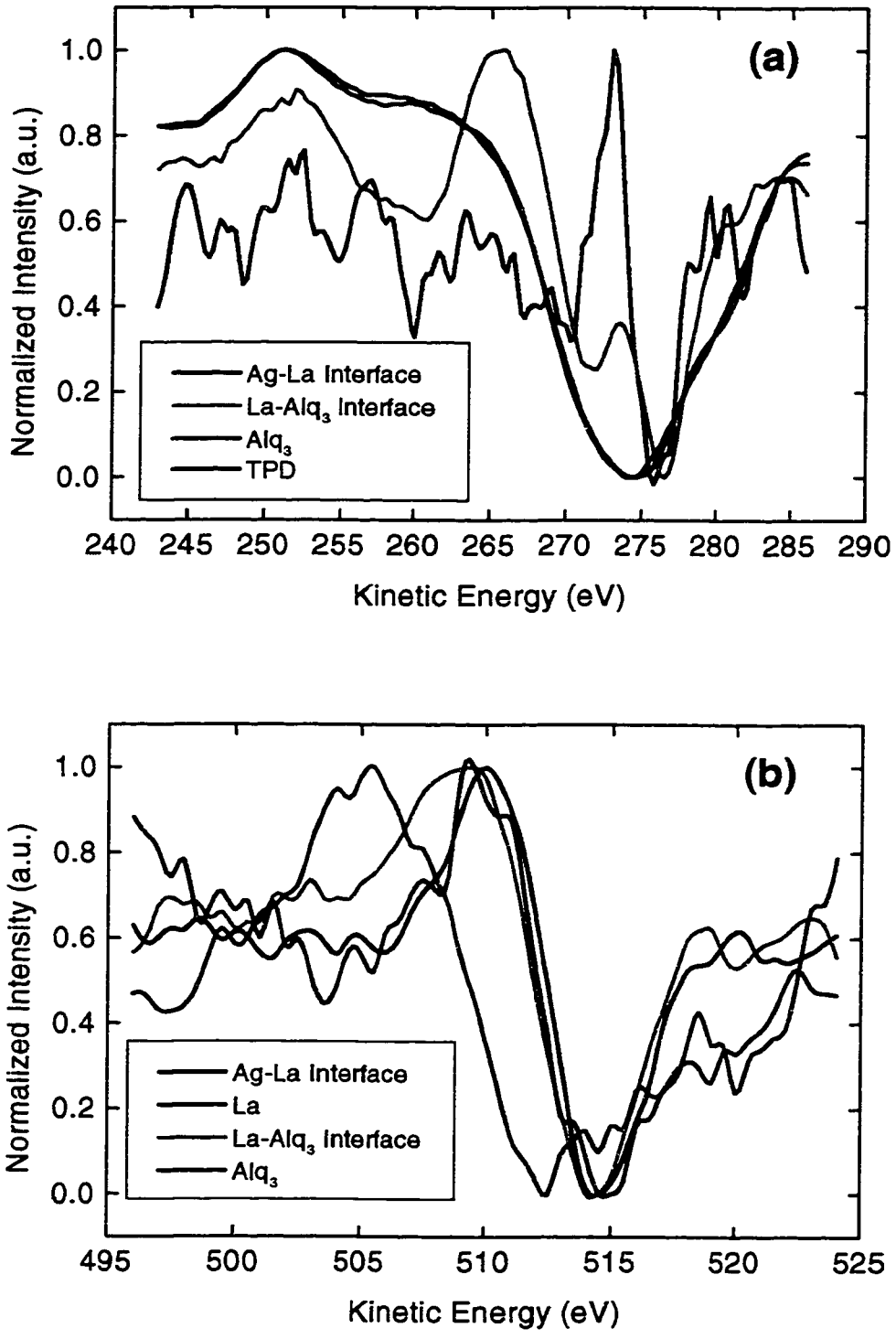

Figure 4.16: (a) Carbon and (b) oxygen elemental analysis taken at various places from sample NRC 238.

Several images were taken of each side of the hole. The origin of the white line that appears to be uniformly deposited throughout the device between the ITO and the TPD remains unknown. Figures 4.18 and 4.19 show enlarged views of this feature.

The thickness values from Figure 4.19 are 124 nm total organic layers (60 nm Alq_3 and 60 nm TPD target) and 331 nm lanthanum and silver (133 nm La and 200 nm Ag target). The unknown layer is approximately 45 nm thick and the ITO layer is fairly thick at 166 nm. All three FEM images of NRC 238 indicate that the silver film has a very rough surface, possibly indicating that the film is not homogeneous although the interfaces appear to be very smooth.

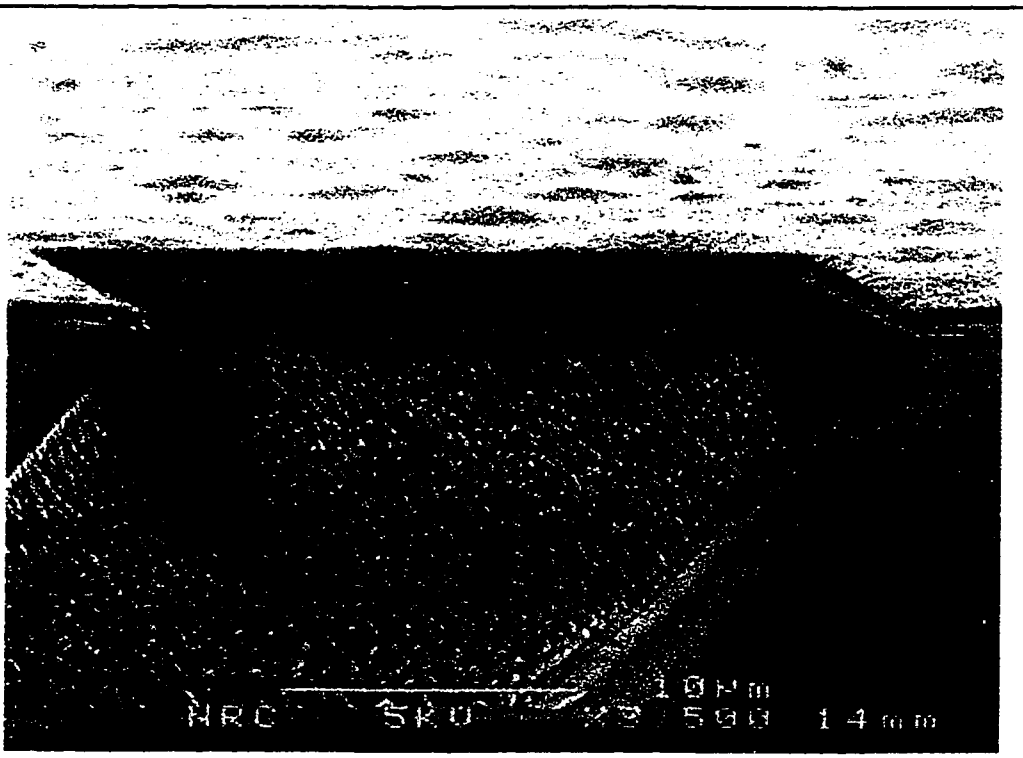

Figure 4.17: Hole bored by the SIMS ion mill into the cleaved side of sample NRC238. Note the surface roughness and the folding of deposited layers on the left corner of the hole.

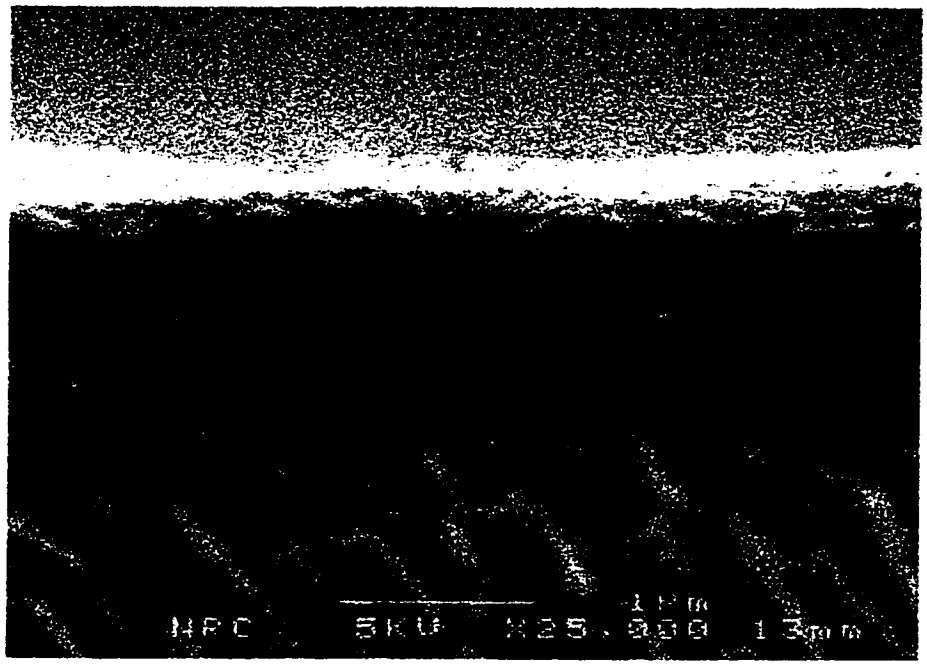

Figure 4.18: Enlargement of the back wall of the hole shown in Figure 4.17. Note the white line that appears to pass through the center of the deposited layers.

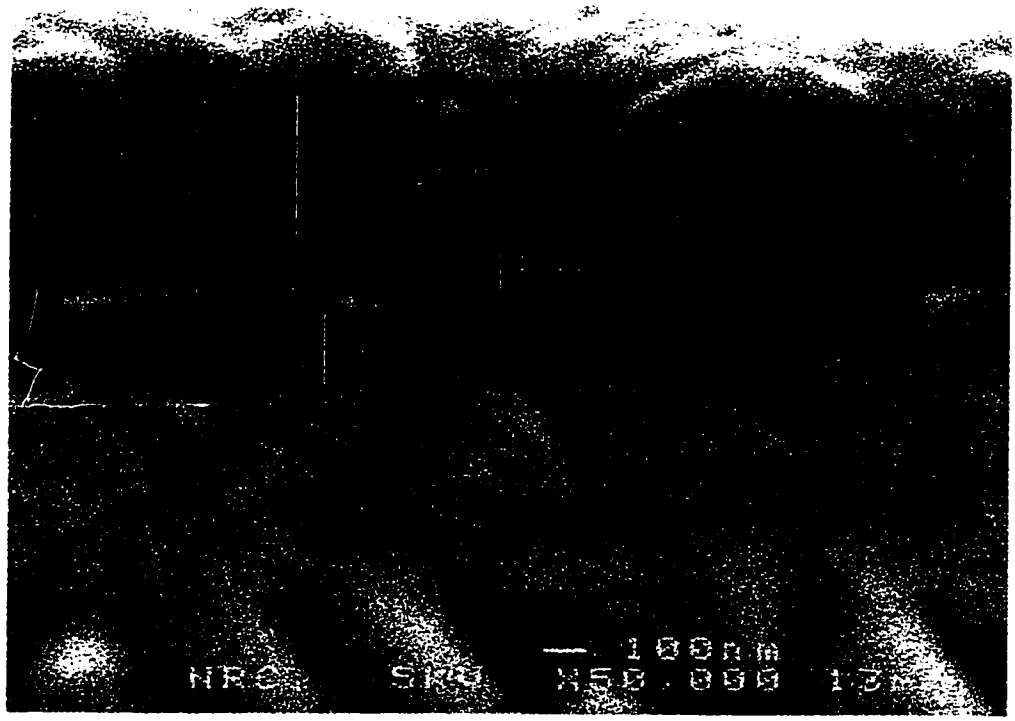

Figure 4.19: High resolution FEM image of the back wall of Figure 4.17. Here we see the thickness of the white line is approximately 45nm thick. Unlike the image for sample NRC 222, we are not able to resolve the La and Ag layers.

4.3.3 Lanthanum/Yttrium Alloy Cathode

Lanthanum/yttrium alloys were deposited by placing an yttrium and a lanthanum piece in a tungsten coil. The lanthanum was placed on top so that it would flow over the yttrium as it melted, alloy and evaporate.

In Figure 4.20, we show the J-L-V characteristics of one of these devices (NRC 241). We can see that the current density was very low until the device failed at approximately 10V. Fitting the J-V data to a TCL model, we find that the trap density is 4.1×10^{18} cm^{-3} and the characteristic trap energy is 0.13 ± 0.01 eV. We can see that the trap energy is about 0.05 eV lower than with pure lanthanum while the trap density is of the same order of magnitude. Using the SCL model, we find that the slope in the SCL

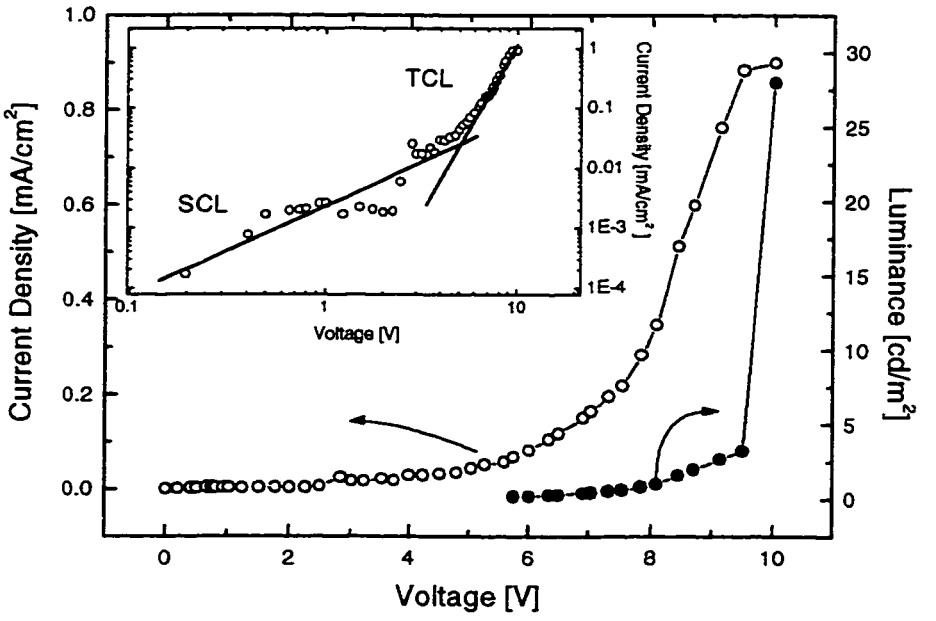

Figure 4.20: J-L-V properties of sample NRC 241 with ~80nm of La/Y alloy cathode. The low luminance values were because of camera misalignment. The inset shows the J-V characteristics on a log-log scale fit to SCL and TCL models. We find that $E_t = 0.13 \pm 0.01$ eV and $N_t = 4.1 \times 10^{18}$ cm^{-3}. Slope in the SCL region was found to be 1.5 ± 0.2.

regime is 1.5 ± 0.2. This is close to the V^2 relationship for SCL currents.

However, the luminance values are vastly underestimated due to misalignment of the CCD camera and the sample. We can see that for the last data point, the geometry of the characterization set was slightly modified and this resulted in an almost 10-fold increase in luminance.

As we had no method of controlling the ratio of yttrium and lanthanum in the alloy, we performed AES and XPS analysis on thermally deposited alloys on a (001) silicon sapphire substrates to determine the La:Y composition ratio.

In Figure 4.21 we show the AES spectrum of a 100nm film of La/Y alloy on a sapphire substrate. The lanthanum and yttrium pieces were placed in HCl to remove surface oxide and to decrease the size of the shots. The carbon signal that is present

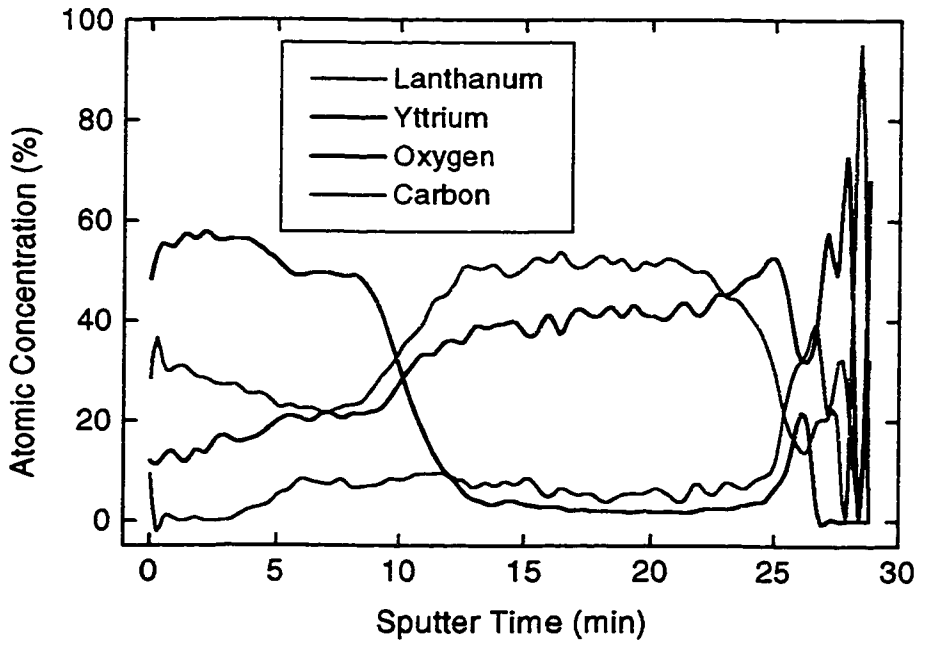

Figure 4.21: AES atomic concentration data for a 100 nm thick film of La/Y alloy.

throughout the profile is most likely due to contamination from within the chamber during deposition – carbon evolved from the turret or the walls due to inadequate cleaning. The high oxygen content that is present in the first third of the profile is due to thermal oxidation of the La-Y alloy. While the alloy was being deposited, the lanthanum to yttrium ratio was nearly 1:1. As the deposition rate decreased, the heat generated by the tungsten filament was enough to cause thermal oxidation of the deposited film. Hence we see a dramatic increase in the oxygen level in the upper part of the film. There also appears to be some contamination on the surface of the sapphire substrate by carbon and oxygen – perhaps from the organic solvent cleaning process.

This would indicate that during growth one must load more lanthanum and/or yttrium than is necessary for the device in order to ensure that the deposition rate does not drop, causing the formation of a surface oxide.

In Figure 4.22 we show an XPS spectrum for a 30 nm thick La/Y film on a (001) silicon substrate. Three trials at different angles of incidence were used to test if the features in the spectrum were confined to the surface only (contamination or a surface oxide) or if they were indeed present throughout the film. As the angle of incidence (with respect to the normal of the sample surface) becomes larger, the x-ray beam will graze the surface and will be more sensitive to surface features. As the angle is decreased, the x-ray beam will penetrate deeper into the film providing more information from within the film. As we can see from the data in table 4.2, the ratio of La_2O_3:La remains approximately 2.0 as the angle is changed. Similarly, the La:Y ratio remains close to unity as the angle is changed, indicating that there are equal amounts of La and Y present in the alloy.

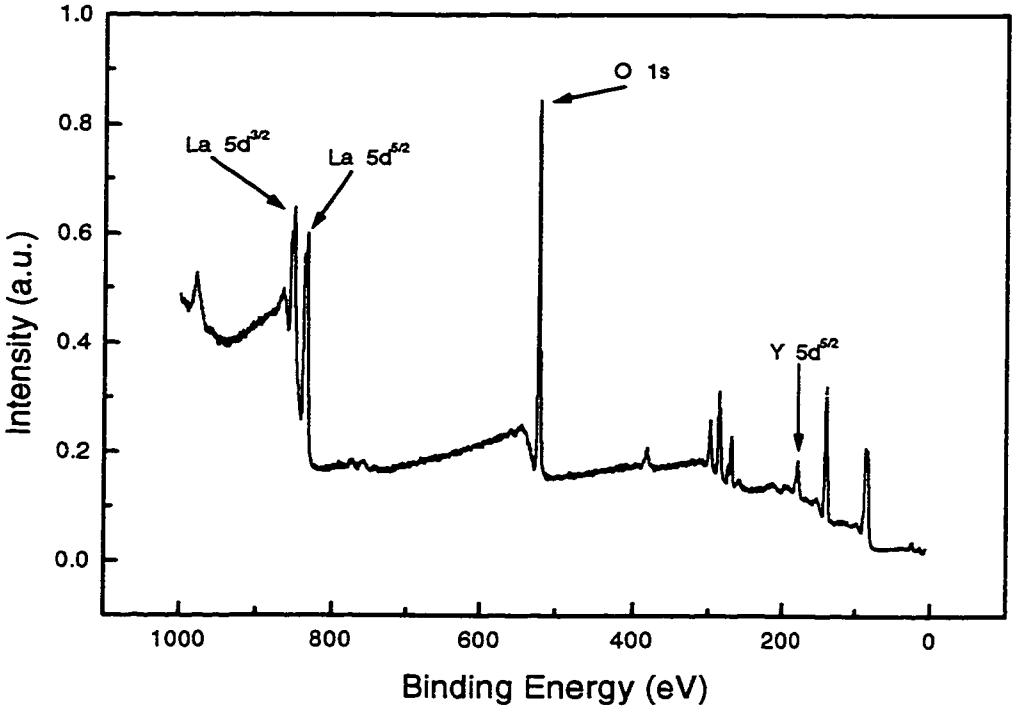

Figure 4.22: XPS spectrum for a 30 nm thick La-Y alloy thin film on (001) silicon.

Angle (degrees)	La $3d^{5/2}$ area (oxide)	La $3d^{5/2}$ position (oxide)	La $3d^{5/2}$ area (metal)	La $3d^{5/2}$ position (oxide)	Ratio (oxide:metal)
30	9325	834.86 eV	5229	838.75 eV	1.8
45	16168	834.86 eV	9067	838.76 eV	1.8
70	31751	834.54 eV	15912	838.70 eV	2.0

Angle (degrees)	Y $3d^{5/2}$ area	Y $3d^{5/2}$ position	La:Y ratio
30	3589	157.25 eV	0.98
45	5745	157.30 eV	1.06
70	10602	157.09 eV	1.09

Table 4.2: XPS data for 30°, 45° and 70° incident angles. La_2O_3:La and La:Y ratios are consistent for all three data sets indicating that there is almost twice as much La_2O_3 as La in the film and that the ratio of La:Y is almost unity, implying that there are near-equal amounts of lanthanum and yttrium in the alloy.

4.4 Pd Anode & Lanthanum Cathode

Even though ITO is an adequate anode, it has many limitations. Devices with palladium anodes were tried because of encouraging preliminary work, but is outside the scope of this work. We present the results of a Pd anode/La cathode device for completeness.

Since palladium has limited transmission in the visible, very thin layers were used – films between 4 and 8nm were deposited with the transmission ranging from approximately 80% for the 4nm thick film to approximately 60% for the 8nm thick film as shown in Figure 2.10. In the device presented here (NRC 240) the palladium layer was about 6 nm thick which corresponds to about 77% transmission at 550 nm.

Figure 4.23 shows the J-V data for this device. Again, no luminance values were obtained because of camera alignment problems and poor light emission in general from the device. It is obvious that there were considerably more shorts present than with the ITO. Poor uniformity of the Pd film may be a significant contributor.

Performing a fit to the TCL region, we obtain E_t = 0.20 ± 0.03 eV and N_t = 5.6×10^{19} cm^{-3}. A fit to the SCL below 2 volts gives a slope of 1.9 ± 0.2, which is consistent with the V^2 model. If we extrapolate the linear fit through the region with the short, we can see that SCL is quite large and is distorted by the presence of shorts.

Since palladium readily absorbs hydrogen, it is possible that when an electric field is applied, the palladium will degas and release the hydrogen into the device, which may cause premature device failure.

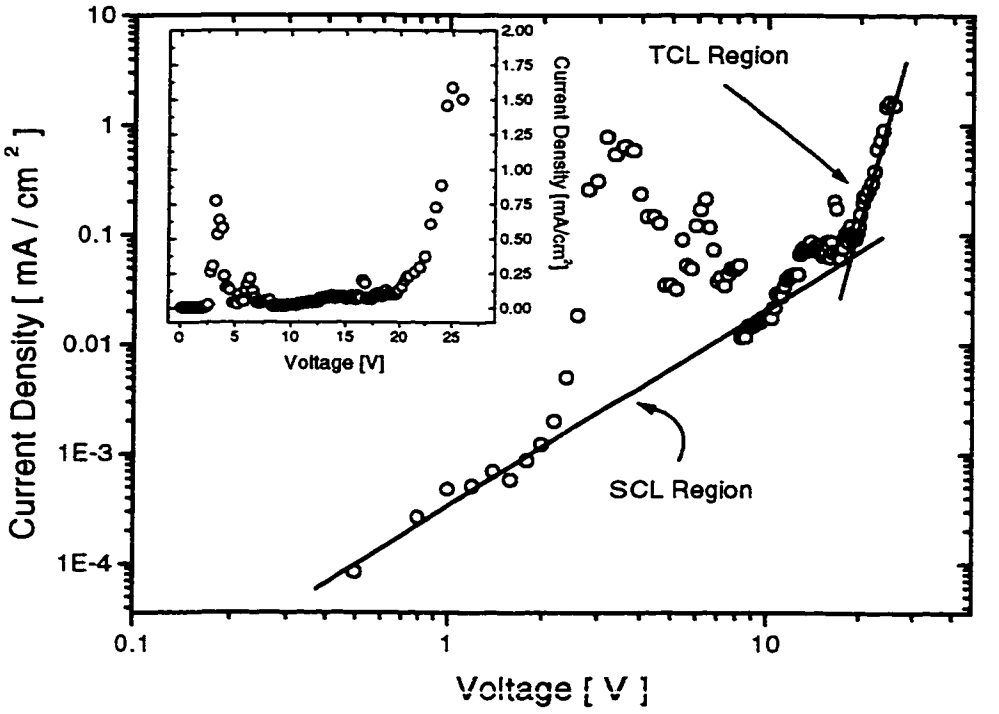

Figure 4.23: J-V characteristics for a 6nm thick Pd anode and 120nm thick La cathode. The TCL region gives E_t = 0.20±0.03 eV and N_t = 5.6x10^{19} cm^{-3}. The SCL region gives a slope of 1.85 ± 0.17 if we ignore the spikes due to shorts. The inset shows the J-V graph on a linear scale with the shorts clearly visible.

5. Conclusions

In the course of this work, we have investigated several aspects of organic light emitting device fabrication; anode surface morphology and materials were briefly explored and cathode materials were extensively studied.

Indium tin oxide was examined as a standard anode. The effect of etching and passivation was examined using scanning electron microscopy and atomic force microscopy. We found that the RMS roughness of the ITO surface was about 1.35nm on average. Palladium was also used as the anode to show that there are alternate materials available. The palladium device had many shorts in the lower voltage regime, indicative of possible discontinuities in the anode. This is not surprising because the rate of deposition of the Pd was very high and the thickness was very low.

The major part of this work focused on the growth, characterization, and analysis of lanthanum-based cathodes used for organic light emitting devices. Pure lanthanum cathodes were deposited and yielded luminescence values over 1000 cd/m^2, low current densities and low turn on voltages. In order to obtain thicker cathode films, the substrate was brought closer to the source with the possible disadvantage of cross contamination of the sources and film inhomogeneity.

Bilayer cathode geometries were studied using lanthanum and silver. These devices exhibited very high current densities and poor luminescence. Auger electron spectroscopy of these devices has shown that there are significant carbide layers present on either side of the lanthanum layer, which are thought to contribute to the high current densities and inhomogeneous light emission. From the Auger electron spectroscopy data, we also observed oxide peaks at the lanthanum interfaces. We postulate that these oxides

are not confined to only the lanthanum-silver devices, but are present in all lanthanum-based devices, including pure lanthanum. In addition to lanthanum's excellent work function matching, the oxide that forms at the organic-cathode interface creates a natural insulating barrier which improves the electron injection efficiency.

Lanthanum yttrium alloys were also examined and the results were comparable to the pure lanthanum cathodes. It was obvious to the eye that the La/Y devices were as bright as the lanthanum ones.

However, due to their instability in air, physical encapsulation techniques must be used in order to manufacture devices with lifetimes appropriate for commercial products. Crude encapsulation may consist of depositing a thick layer of one of the organic materials (preferably TPD due to its lack of oxygen) over the metal to provide a barrier against oxygen and water. A thick layer of parylene can also be deposited over the entire device to seal it, and is air stable. This has been shown to increase the device's lifetime from hours to several days. Other methods include the use of epoxy between two pieces of glass to seal the device, epoxy with embedded glass beads, and a hermetically sealed enclosure around the device which contains an overpressure of dry nitrogen gas. Typically, this last method is used in conjunction with one of the previously mentioned encapsulation techniques.

Further work in this area will include the study of new air-stable alloys with appropriate work functions and more efficient deposition techniques, which will allow better homogeneity of the metal layer and reduce the formation of thermal surface oxides.

6. References

1 M. Pope, H. Kallmann, and P. Magnante, *J. Chem. Phys* **38,** 2540 (1963).

2 J. Dresber, *RCA Rev.* **30,** 322 (1969).

3 C. W. Tang and S. A. Van Slyke, *Appl. Phys. Lett.* **51,** 913 (1987).

4 N. Peyghambarian, C. Spiegelberg, G. E. Jabbour, A. Schulzgen, D. L. Mathine, and B. Kippelen, in *SPIE's 43rd Annual Meeting* (San Diego, 1998).

5 B. Williams, *Personal Communication* (1997).

6 M. Pope and C. E. Swenbery, *Electronic Processes in Organic Crystals* (Oxford, 1982).

7 F. Gutmann, H. Keyzer, and L. E. Lyons, *Organic Semiconductors* (Robert. E. Krieger Publishing Company, Malabar, 1983).

8 J. J. M. Halls, C. A. Walsh, N. C. Greenham, E. A. Marsegila, R. H. Friend, S. C. Moratti, and A. B. Molmes, *Nature* **376,** 498 (1995).

9 J. P. Wheeler, in *Photonics Spectra* (1997), p. 130.

10 A. R. Brown, D. D. C. Bradely, J. H. Burroughes, R. H. Friend, N. C. Greenham, P. L. Burn, A. B. Holmes, and A. Kraft, *Appl. Phys. Lett.* **61,** 2793 (1992).

11 E. I. Haskal, in *SPIE's 43rd Annual Meeting* (San Diego, 1998).

12 C. Adachi, K. Nagai, and N. Tamoto, *Appl. Phys. Lett.* **66,** 2679 (1995).

13 C. W. Tang, S. A. Van Slyke, and C. H. Chen, *J. Appl. Phys.* **65,** 3610 (1989).

14 P. E. Burrows, Z. Shen, V. Bulovic, D. M. McCarty, and S. R. Forrest, *J. Appl. Phys.* **79,** 7991 (1996).

15 S. Aratani, C. Zhang, K. Pakbar, S. Hoger, F. Wudl, and A. J. Heeger, *J. Electron. Mater.* **22,** 745 (1993).

16 N. F. Mott and E. A. Davis, *Electronic Processes in Noncrystalline Solids* (Clardendon Press, Oxford, 1979).

17 M. Nechtschein, *Organic Conductors: Fundamentals and Applications* (Marcel Dekker , Inc., New York, 1994).

18 A. Rose, *Phys. Rev.* **97,** 1538 (1955).

19 M. A. Lampert, *Phys. Rev.* **103,** 1648 (1956).

20 R. W. Smith and A. Rose, *Phys. Rev.* **97,** 1531 (1955).

21 P. Mark and W. Helfrich, *J. Appl. Phys.* **33,** 205 (1962).

22 J. Kalinowski, N. Camaioni, P. DiMarcon, V. Fattori, and G. Giro, *Int. J. Electronics* **81,** 377 (1996).

23 J. Goldlewski and J. Kalinowski, *Jap. J. Appl. Phys.* **28,** 24 (1989).

24 R. H. Fowler and L. Nordheim, *Proc. R. Soc. London Ser* **A 119,** 173 (1928).

25 L. Esaki, *Tunneling Phenomena in Solids* (Plenum, New York, 1969).

26 J. Kalinowski, P. DiMarco, N. Camaioni, V. Fattori, W. Stampor, and J. Duff, *Synthetic Metals* **76,** 77 (1996).

27 J. Kalinowski, in *Polymers and Other Advanced Materials: Emerging Technologies in Business Opportunities*, edited by P. N. Prasad, E. Mark, and J. F. Fung (Plenum, New York, 1996), p. 361.

28 A. R. Brown, D. D. C. Bradley, J. H. Burroughes, R. H. Friend, N. C. Greenham, P. L. Burn, A. B. Holmes, and A. Kraft, *Appl. Phys. Lett.* **61,** 2793 (1992).

29 L. J. Rothberg and A. J. Lovinger, *J. Mater. Res.* **11,** 3174 (1996).

30 M. Yan, L. J. Rothberg, F. Papadimitrakopoulos, M. E. Galvin, and T. M. Miller, *Phys. Rev. Lett.* **72,** 1104 (1994).

31 S. A. Van Slyke and C. W. Tang, *Digest of LEOS Summer Topical Meetings*, 3 (1995).

32 R. Kersting, U. Lemmer, R. F. Mahrt, K. Leo, H. Kurtz, H. Bässler, and E. O. Göbel, *Phys. Rev. Lett.* **70,** 3820 (1993).

33 M. Yan, L. J. Rothberg, F. Papadimitrakopoulos, M. E. Galvin, and T. M. Miller, *Phys. Rev. Lett.* **73,** 744 (1994).

34 V. G. Kozlov, V. Bulovic, and S. R. Forrest, *Appl. Phys. Lett.* **18,** 2575 (1997).

35 P. E. Burrows, V. Bulovic, S. R. Forrest, L. S. Sapochak, D. M. McCarty, and M. E. Thompson, *Appl. Phys. Lett.* **65,** 2922 (1994).

36 H. Antoniadis, M. R. Hueschen, J. N. Miller, R. L. Moon, D. B. Roitman, and J. R. Sheats, *Macromol. Symp.* **125,** 59 (1997).

37 S. A. Van Slyke, C. H. Chen, and C. W. Tang, *Appl. Phys. Lett.* **69,** 2160 (1996).

38 E.-M. Han, L.-M. Do, Y. Niidome, and M. Fujihira, *Chemistry Letters*, 5, 969 (1994).

39 C. W. Tang, in *1996 SID Int. Symp. Digest of Technical Papers* (SID, San Diego, 1996), p. 181.

40 H. Aziz, Z. Popovic, C. P. Tripp, N.-X. Hu, A.-M. Hor, and G. Xu, *Appl. Phys. Lett* **72,** 2642 (1998).

41 C. Kittel, *Introduction to Solid State Physics*, 7th Edition ed. (John Wiley & Sons, Toronto, 1996).

42 Y. Park, V. Choong, Y. Gao, B. R. Hsieh, and C. W. Tang, *Appl. Phys. Lett.* **68,** 2699 (1996).

43 I. D. Parker, *J. Appl. Phys.* **75,** 1656 (1994).

44 T. Ishida, H. Kobayashi, and Y. Nakato, *J. Appl. Phys.* **73,** 4344 (1993).

45 *Goodfellow Catalog* (1996-1997).

46 V. L. Rideout, *Solid State Electronics* **18,** 541 (1975).

47 S. M. Sze, *Physics of Semiconductor Devices*, Second Edition ed. (John Wiley & Sons, Toronto, 1981).

48 E. H. Rhoderick, *IEE Proceedings-I Solid-State and Electron Devices* **129,** 1 (1982).

49 T. B. Brantly, L. E. Contois, and C. J. Fox, (US 3,658,520, 1972).

50 R. G. Kepler, P. M. Beeson, S. J. Jacobs, R. A. Anderson, M. B. Sinclair, V. S. Valencia, and P. A. Cahill, *Appl. Phys. Lett.* **66,** 3618 (1995).

51 F. E. Lytle, D. R. Storey, and M. E. Juricich, *Spectrochimica Acta* **29A,** 1357 (1973).

52 D. Z. Garbuzov, V. Bulovic, P. E. Burrows, and S. R. Forrest, *Chem. Phys. Lett.* **249,** 433 (1996).

53 C. Hosokawa, H. Tokailin, H. Higashi, and T. Kusumoto, *Appl. Phys. Lett.* **60,** 1220 (1992).

54 J. C. C. Fan and J. B. Goodenough, *J. Appl. Phys.* **48,** 3524 (1977).

55 T. Osada, T. Kugler, P. Bröms, and W. R. Salaneck, *Synthetic Metals* **96,** 77 (1998).

56 P. Nath and R. F. Bunshah, *Thin Solid Films* **69,** 63 (1980).

57 J. C. C. Fan, F. J. Bachner, and G. H. Foley, *Appl. Phys. Lett.* **31,** 773 (1977).

58 S. A. Bashar, Ph.D. Thesis, King's College London, University of London, 1998.

59 K. Sreenivas, T. S. Rao, A. Mansnigh, and S. Chandra, *J. Appl. Phys.* **57,** 384 (1985).

60 J. Szczyrbowski, A. Dietrich, and H. Hoffmann, *Phys. Stat. Sol. A* **78,** 243 (1983).

61 M. Higuchi, S. Uekusa, R. Nakano, and K. Yokogawa, *Jpn. J. Appl. Phys.* **33,** 302 (1994).

62 N. Balasubramanian and A. Subrahmanyam, *Mat. Sci. Eng* **B1,** 279 (1988).

63 J. Bregman, Y. Shapira, and H. Aharoni, *J. Appl. Phys.* **67,** 3750 (1990).

64 H. Haitjema and J. J. P. Elich, *Thin Solid Films* **205,** 93 (1991).

65 J. H. Weaver and R. L. Benbow, *Phys. Rev. B* **12,** 3509 (1975).

66 M. Born and E. Wolf, *Principles of Optics*, 6th ed. (Pergamon Press, Toronto, 1980).

67 *Edwards FTM5 Thickness Monitor Manual.*

68 C. Py, *Personal Communication* (1998).